Impacts of Predicted Liquid Fraction and Multiple Ice-Phase Categories on the Simulation of Hail in the Predicted Particle Properties (P3) Microphysics Scheme

Jason A. Milbrandt[1*], Hugh Morrison[2], and Mélissa Cholette[1]

[1]Meteorological Research Division, Environment and Climate Change Canada, Dorval, Quebec, Canada

[2]NSF National Center for Atmospheric Research, Boulder, Colorado, United States of America

*Corresponding author: Jason A. Milbrandt (jason.milbrandt@ec.gc.ca), Environment and Climate Change Canada, 2121 Transcanadienne, Dorval, QC, Canada, H9P 1J3.

Key Points:

- Predicting the liquid fraction improves the parameterization of melting and results in reduced hail sizes.
- The use of multiple free ice-phase categories reduces the dilution of bulk physical properties of ice and increases hail sizes.
- With recent updates, the Predicted Particle Properties bulk microphysics scheme is well-suited for modeling hailstorms.

Abstract

Since its inception in 2015, the Predicted Particle Properties (P3) bulk microphysics scheme has undergone several major developments. Ice is now represented by a user-specified number of freely-evolving (non-prescribed) categories; the liquid fraction of particles is predicted, thereby allowing for mixed-phase particles and improved process rates; and the scheme is triple-moment, which allows the size spectral width to vary independently. As such, P3 is now capable of representing key properties and microphysical processes that are important for hail. In this study, the impacts of some new capabilities of P3 on the simulation of hail amounts and sizes are examined in the context of quasi-idealized, high-resolution (200-m isotropic grid spacing) simulations using a cloud-resolving model. Two hailstorm cases are simulated, one from Oklahoma (US) and the other from Alberta (Canada), each initialized from qualitatively different soundings. For each case, sensitivity tests are conducted to examine the impacts of 1) the predicted liquid fraction, and 2) the number of free ice-phase categories (varied between one and four). Predicted liquid fraction leads to a more realistic treatment of melting and shedding, which decreases mean ice (hail) sizes during melting compared to the original P3 scheme. In contrast, with an increasing number of ice-phase categories, the problem of property dilution is mitigated, resulting in greater quantities and larger sizes of hail reaching the surface. It is argued that the latest version of the P3 scheme is now capable of realistically representing the major microphysical processes involved in the initiation, growth, and decay of hail.

Plain Language Summary

The Predicted Particle Properties (P3) scheme is a piece of computer code, used in atmospheric numerical models, that calculates the bulk effects of cloud processes that ultimately lead to precipitation. Since its inception in 2015, the P3 scheme has undergone several major developments. Ice-phase particles are now represented by a user-specified number of freely evolving generic categories; P3 now predicts the liquid fraction which allows for mixed-phase particles and more accurate calculations of physical processes; and there is flexibility in representing the distribution of ice particle sizes. With these features, P3 is now capable of simulating the physical processes related to the growth and decay of hail. In this study, the impacts of the new features on the simulation of hail were examined using a fine-scale, detailed numerical model capable of simulating individual storms. Two hailstorm cases were simulated, each with different pre-storm environments in order to illustrate the robustness of the conclusions. The predicted liquid fraction was shown to improve the simulation of hail melting and resulted in smaller hail at the surface. In contrast, the use of two or more ice-phase categories allowed for the simulation of larger hail sizes.

1 Introduction

A major component of an atmospheric model is the bulk microphysics scheme (BMS), which parameterizes the effects of grid-scale clouds and precipitation. Despite the existence of more detailed approaches, bin-resolving and Lagrangian super-particles schemes, BMSs continue to play important roles in research and are ubiquitous in operational numerical weather and climate prediction models. This is expected to continue into the foreseeable future. Since ice was introduced into single-moment schemes decades ago (e.g., Rutledge & Hobbs, 1983), the treatment of ice-phase microphysics has become increasingly sophisticated. Over the years, more categories were added to expand the range of properties of frozen particles represented in models, in particular terminal fall speeds (e.g. Lin et al., 1983). Detailed two-moment schemes later become popular (e.g. Ziegler, 1985; Murakami et al., 1990; Ferrier, 1994; Meyers et al., 1997; Reisner et al., 1998; Seifert & Beheng, 2006; Morrison et al., 2005; Morrison et al., 2009). Three-moment schemes then followed (Milbrandt & Yau, 2005a,b; Yang & Yau, 2008; Dawson et al., 2014; Loftus et al., 2014; Chen & Tsai, 2016). More recently, the prognostic volume mixing ratio for rimed ice categories (graupel and hail) was included in some schemes, which allows for the prediction of the bulk particle density (Mansell et al., 2010; Milbrandt & Morrison, 2013; Jensen et al., 2023; Park et al., 2024). Tsai & Chen (2020) developed a BMS which, in addition to bulk density, predicts the shape evolution of the ice-phase categories. Thompson & Eidhammer (2014) included prognostic aerosols, which ultimately is important in determining droplet sizes; this in turn impacts the rime density in the most recent version of this scheme, which now includes prognostic graupel density. With all of these predictive aspects, BMSs are now capable of simulating the key microphysical processes involved in the production and growth of hail.

Despite many advances, most BMS are still constructed around the original approach of using pre-defined ice-phase categories (e.g. “snow”, “graupel”, etc.) usually with fixed parameters to define or diagnose the values of bulk physical properties. This traditional approach has some inherent and insurmountable weaknesses. First, the properties of natural ice particles vary considerably. This is in contrast with liquid drops and droplets, whose density is constant and with spherical shape (except for large drops). Perhaps most importantly, the traditional approach requires the parameterized process of conversion between categories; this process is unphysical and is purely a necessary artifact of the construction of the scheme. It is therefore unconstrained by observations or theory and its closure assumptions introduce model sensitivity (Morrison et al., 2020). Note that these problems are equally inherent to most bin microphysics schemes, which is illustrated clearly in Xue et al. (2017).

An alternative to traditional, pre-defined ice category-based schemes is the property-based approach, which uses one or more ice-phase categories that do not correspond a priori to a particular ice type. That is, categories are not assigned a type with corresponding fixed parameters, but rather each category includes a set of prognostic variables from which physical properties can be derived and vary continuously in time and space. The first property-based microphysics scheme can probably be credited to Hashino & Tripoli (2007), though this was a bin scheme. The Predicted Particle Properties (P3) scheme was introduced by Morrison & Milbrandt (2015), who proposed the concept of a "free" (freely evolving) bulk ice-phase category. Jensen et al. (2017) also constructed a property-based bulk scheme called Ice-Spheroids Habit Model with Aspect-Ratio Evolution (ISHMAEL), with a unique capacity to predict the evolution of the aspect ratios of ice crystals. To our knowledge, these are the two only property-based BMSs that have been developed that completely eschew traditional ice categories.

Although the P3 scheme was originally constructed as a proof of concept, it initially performed well against detailed, mature, well-calibrated, traditional BMSs. This was true for both historic case studies (Morrison et al., 2015) and in a real-time experimental numerical weather prediction (NWP) context (see Milbrandt et al., 2021). It was (and is) also computationally efficient due in part to its extensive use of pre-computed lookup tables during run time (Morrison et al., 2015). It has since been interfaced with several mesoscale and large-eddy simulation (LES) models; it has been used operationally since 2018 in the 2.5-km deterministic NWP system of Environment and Climate Change Canada (ECCC) (Milbrandt et al., 2016; Milbrandt et al., 2018) and it is available in the Weather Research and Forecasting model (WRF; Skamarock et al., 2008) and the Energy Exascale Earth System Model (E3SM) climate model (Wang et al., 2021). Since its inception, P3 has undergone several major developments. This includes the generalization to multiple ice-phase categories (Milbrandt & Morrison, 2016), prognostic liquid fraction of particles (Cholette et al., 2019), a triple-moment representation of ice (Milbrandt et al., 2021), and a diagnostic subgrid-scale cloud fraction (Jouan et al., 2020). A triple-moment rain version was also developed (Paukert et al., 2019) though this was not incorporated into the main P3 code stream.

Although the P3 scheme is now quite mature and its representation of ice is highly versatile, some aspects have not yet been examined with regards to their impacts on the simulation of hail. In a study using idealized supercell simulations, Johnson et al. (2019) compared the performance of P3 to that of two detailed traditional BMSs and found P3 to perform poorly in comparison for the simulation of dual-polarization radar signatures for hail. These deficiencies were alleviated by the introduction of triple-moment ice (and also improved for a modified double-moment ice configuration) in Milbrandt et al. (2021), which relaxed the restriction of mean ice sizes by varying the particle size spectral width and controlling gravitational size sorting. The impacts of other potentially important recent innovations to P3 have not yet been explored.

The goal of this study, therefore, is to examine the following question: What are the impacts on the simulation of hail from 1) the predicted liquid fraction, and 2) multiple free ice categories? This is examined using quasi-idealized high-resolution (200-m grid spacing) cloud model simulations using the latest version (v5) of P3 for two deep convective hail-producing storms in different environments.

The remainder of the paper is organized as follows: Section 2 describes the experimental design, including the cloud model configuration and the two idealized hailstorm cases. Section 3 summarizes the control simulations for the two cases. Section 4 presents the results of two sets of sensitivity experiments, one looking at the effects of liquid fraction and the other on using different numbers of ice categories. Discussion is provided in section 5 with concluding remarks in section 6.

2 Experimental design

2.1 Overview of the P3 scheme

A complete description of the original single-category version of the P3 scheme is provided in Morrison & Milbrandt (2015) and an overview of the most recent version (at the time of writing), with details on how triple-moment ice and predicted liquid fraction were combined, is given in Cholette et al. (2023). The liquid-phase component of P3 is a standard two-category ("cloud droplets" and "rain"), two-moment (prognostic mass and number) formulation, with a gamma particle size distribution (PSD) for each category. Ice is represented with a user-specified number (nCat; all symbols are defined in Table A1) of free ice-phase categories. The PSD of each ice category is also represented by a gamma function. For all hydrometeor categories, the PSD is of the form

$$N(D) = N_0 D^{\mu} e^{-\lambda D}, \tag{1}$$

where $N(D)$ is the number of particles between D and $D + dD$, D is the equivalent diameter, and N_0, λ , and μ are the intercept, slope, and shape parameters, respectively (see Table 1 for units). There are between four and six prognostic mixing ratio variables per ice category: the total mass ($Q_{i,tot}$), rime mass ($Q_{i,rim}$), total number ($N_{i,tot}$), rime volume ($B_{i,rim}$), and optionally the sixth moment (Z_i) and liquid mass accumulated on ice ($Q_{i,liq}$). Since all of these quantities are mixing ratios, they are conserved and can be advected and diffused appropriately. Note, $Q_{i,tot}$ is the total mass of a given ice (in general, mixed-phase) category, n, equal to the sum of $Q_{i,liq}$, $Q_{i,rim}$, and the deposition mass (which can be computed but is not actually a prognostic variable) for the category. The actual total mass of ice- or mixed-phase particles (e.g. in a grid element) is the sum of all $Q_{i,tot}(n)$ for n from 1 to $nCat$.

From these prognostic variables, various bulk physical properties can be computed, including the rime fraction (F_{rim}), liquid fraction (F_{liq}), density (ρ_i), mass-weighted mean terminal fall speed (V_m) (and also the number-weighted and sixth moment-weighted fall speeds, for the sedimentation of $N_{i,tot}$ and $Z_{i,tot}$, respectively), and mass-weighted mean diameter (D_m). In this study, we also examine the maximum hail size, $D_{h,max}$, which can be diagnosed from the tail of the PSD following the method described in Milbrandt et al. (2021).

An overview of the representation of ice (and mixed-phase particles) and the major growth/decay processes is depicted in Fig. 1. Pristine crystals can be initiated from either primary nucleation, homogeneous freezing of cloud droplets, or secondary ice production (SIP).

Currently the only SIP mechanism included is rime splintering, but in the near future other modes will be added, such as the fragmentation of freezing drops, which was shown to be important for tropical convection (see Qu et al., 2022). Ice can grow (or decay) from deposition (sublimation), undergo aggregation, both within a given ice category and between categories, and grow gradually from riming. With the predicted liquid fraction, liquid can remain on the particles during wet growth and possibly re-freeze before being shed as rain. During melting, the small ice sizes in the PSD melt instantly to rain while the remaining ice mass is retained as partially-melted mixed-phase particles. Shedding during melting and wet growth is computed explicitly with the prediction of liquid fraction. Mixed-phase particles can also re-freeze if they fall or are transported into subfreezing air. As in the original scheme, rain can freeze to solid (maximum-density) ice via either immersion freezing or through collisions with existing ice. Thus, hail embryos can originate from either graupel or frozen drops, and since freezing has a drop-size dependence there is an indirect dependence on aerosols for the origin of hail embryos. (Currently P3 does not have prognostic aerosol concentrations, though this will be implemented in the near future.)

Table 1. List of simulation configurations. Runs are named with the convention *case-configuration*. The *case* is either "OK" or "AB" to denote the Oklahoma [date] or Alberta [date] case, respectively. The control ("CTR") configuration has predicted liquid fraction off and uses one ice category. "LF" denotes liquid fraction on. For multi-ice-category runs, (x) in "(x)CAT" indicates the number of ice categories, which is implicitly 1 if not indicated. "MOD" denotes modified; see main text for details. All simulations use 3-moment-ice.

Run name	Liq-Frac	nCat
OK-CTR	off	1
OK-LF	on	1
OK-CTR-MOD	off	1
OK-LF-MOD	on	1
OK-LF-2CAT	on	2
OK-LF-3CAT	on	3
OK-LF-4CAT	on	4
AB-CTR	off	1
AB-LF	on	1
AB-LF-2CAT	on	2
AB-LF-3CAT	on	3
AB-LF-4CAT	on	4

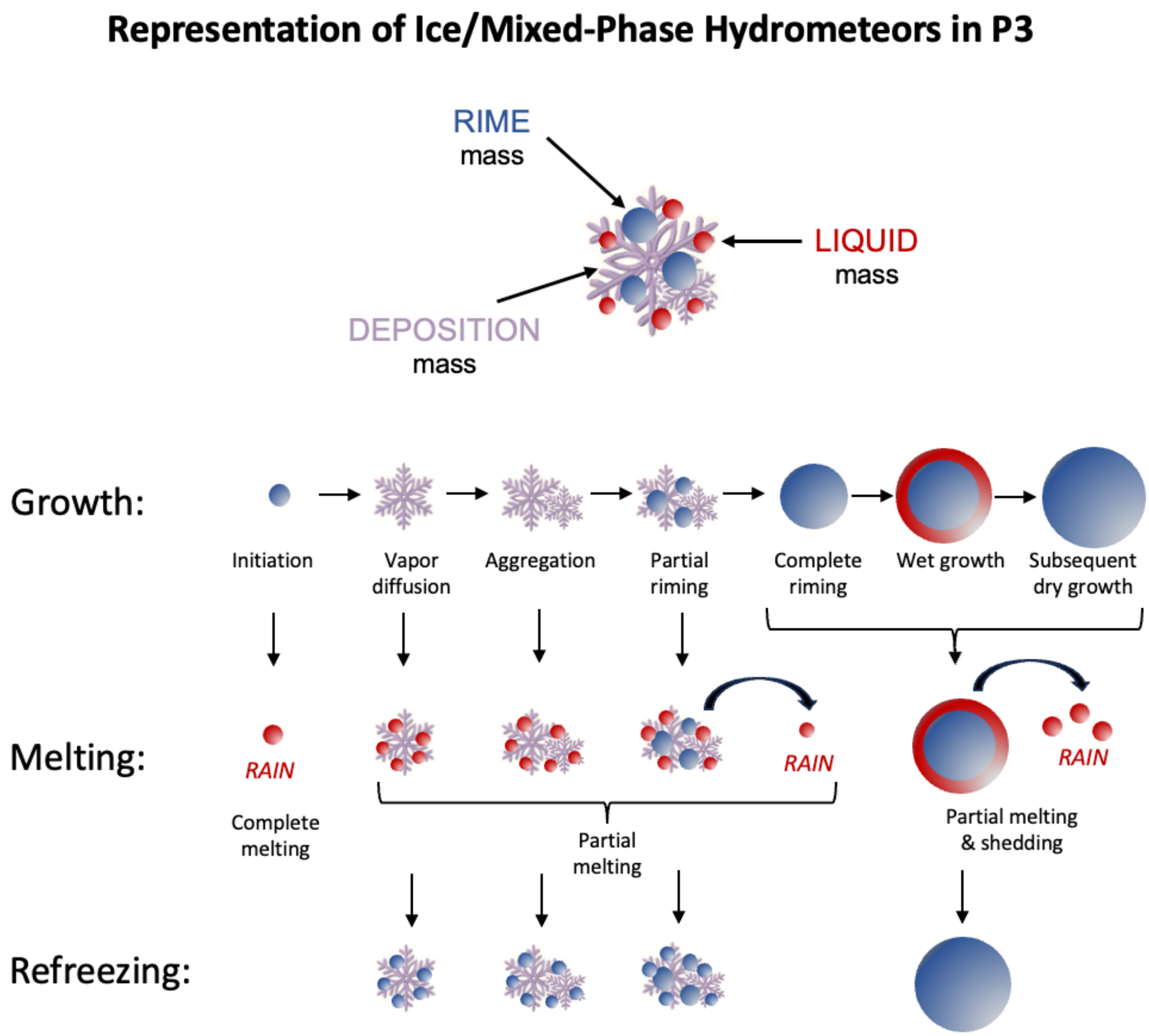

Figure 1. Depiction of the representation of ice-phase and mixed-phase hydrometeors and the main microphysical processes related to ice in P3.

2.2 Summary of idealized simulations

In order to establish robustness of the results, this study examined two hailstorm cases, each with different geographical locations and pre-storm environments. The first is from Oklahoma, USA on 1 June 2008. The observed storm had a warm cloud base, implying an increased likelihood of predominantly frozen-drop hail embryos (Young 1993), high CAPE, and was observed to produce hail sizes at the surface up to 10 cm. This was also the case used in Milbrandt et al. (2021). The second case was from Alberta, Canada on 13 June 2020. This case had a colder cloud base, implying more likelihood of graupel embryos, relatively lower CAPE, yet the observed storm produced a prolific quantity of large hail. The initial sounding for the Alberta case also had stronger mid-to-upper-level vertical shear. The two cases are hereafter referred to as the OK (Oklahoma) and AB (Alberta) cases.

This study is done through examination of quasi-idealized cloud-resolving numerical simulations using the Cloud Model 1 (CM1) model (Bryan & Fritsch, 2002). CM1 is a nonhydrostatic fluid flow model, commonly used to simulate various atmospheric phenomena. We used the compressible dynamics option with sub-time steps for acoustic modes and 5th order advection of scalars using the Weighted Essential Non-Oscillatory scheme (Balsara & Shu, 2000). All simulations used a 200-m isotropic grid spacing and open lateral boundary conditions. The domain sizes were 1000 x 1000 horizontal grid points for OK and 1250 x 1250 for AB, both with 100 vertical levels. The model time step was 2 s. A Rayleigh damping layer was applied to the uppermost 5 km of the model with a damping timescale of 1/300 s^{-1} toward the base state sounding. The upper and lower boundaries were free slip and surface heat fluxes were zero. Horizontally homogeneous initial conditions were used, based on a single sounding for each case (see below). Subgrid-scale mixing used the 1.5 order prognostic turbulent kinetic energy method similar to Deardorff (1980). Radiation and all other physical processes besides microphysics were neglected. Convection was initiated using the vertical motion nudging method of Naylor & Gilmore (2012), with an ellipsoidal region (with a horizontal radius of 15 km and a vertical radius of 1500 m) of vertical motion (peaking at 10 m s^{-1} in the center), with an inverse e-folding time of 0.5 s^{-1}, and nudging decreasing to zero over 20 min. For each case, a control configuration was run along with sensitivity tests related to prediction of liquid fraction and the number of ice-phase categories. All simulations examined in this study are listed in Table 1.

The soundings used to initiate each case, shown in Fig. 2, were taken from operational NWP models. The OK sounding was extracted from the 0100 UTC 1 June 2008 Rapid Update Cycle (RUC) analysis near the region of the initiation of the observed storm (see Milbrandt et al., 2021 and references therein). The AB case was initialized from a 6-h model forecast sounding from ECCC's Regional Deterministic Prediction System (RDPS), valid at 0000 UTC 14 June 2020, near the city of Calgary, near the initiation region of the storm. The temperature and humidity profiles were modified slightly to prevent initial instabilities. Also, the mean 0-6 km wind (the approximate storm translation speed) was subtracted from the sounding winds such that the model storms remained approximately in the domain center throughout the simulations. While a detailed examination of the simulations is provided in the following section, an illustration of the model storms for the control (CTR) runs for each case is shown in Fig. 3, with qualitative comparisons to radar observations. This is not intended to serve as a verification per se, but simply as an illustration of the overall realism of the simulated hailstorms. For the OK case, the combination of $Z_H > 35$ dBZ with $Z_{DR} < 0.5$ dB in the observed storm (Fig. 3, top right panels) is a dual-polarization radar signature for the presence of hail (e.g., Kumjian et al., 2010). The model storm (OK-CTR) has a similar reflectivity structure with the presence of hail (high-density ice) along the right flank. For the AB case, the reflectivity of the observed storm (Fig. 3, bottom right panel) had high values (> 60 dBZ) along the right flank near the surface (0.4° plan position indicator [PPI]), indicative of hail at the surface. The model storm (AB-CTR; Fig. 3, bottom-left panel) has a reasonably realistic reflectivity structure with a hail along the right edge of the reflectivity core. Thus, the model simulations for the two cases appear to be sufficiently realistic in terms of reflectivity structure and their production of hail at the surface that we can confidently use this model framework to examine the impacts of details in the microphysics scheme for the simulation of hail through model sensitivity tests.

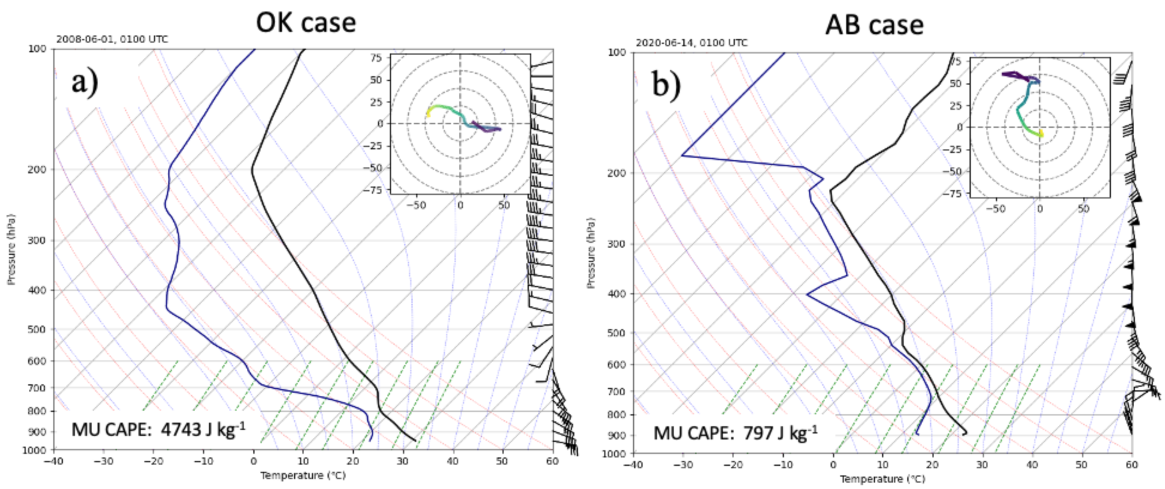

Figure 2. Initial soundings and hodographs for a) OK case, valid at 0100 UTC 1 June 2008, and b) AB case, valid at 0100 UTC 14 June 2020. See main text for additional details. Sounding plots were created using MetPy. Winds are in knots with conventional meaning for the barbs.

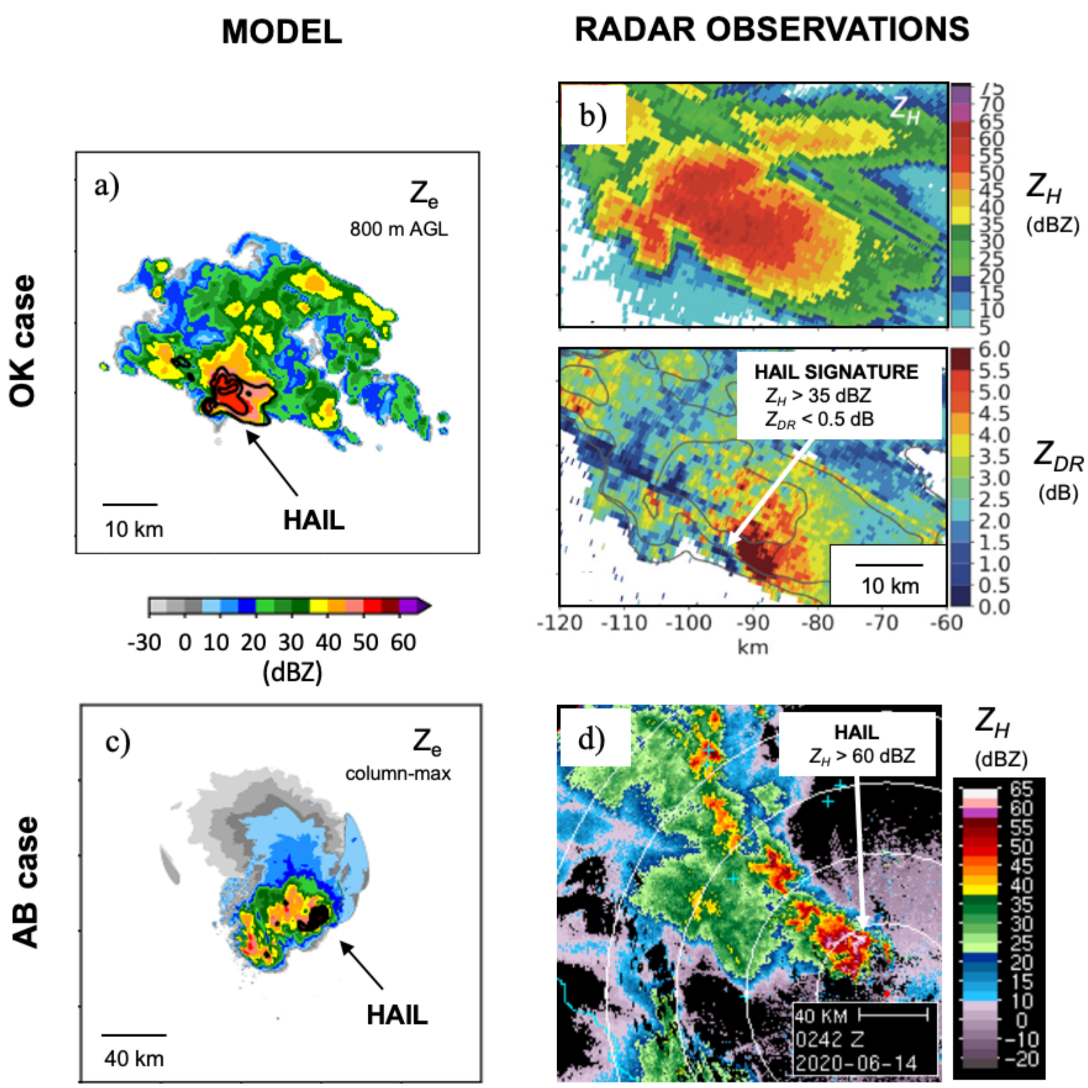

Figure 3. a) Low-level (800 m) Z_e (shading) and $Q_{i,tot}$ (black contours) from OK-CTR (50 min). b) Horizontal (Z_H) and differential (Z_{DR}) reflectivity from operational radar (see Milbrandt et al. 2021 and references therein for details). c) $Z_{e,c}$ (shading) and lowest-level $Q_{i,tot}$ (black contours) from AB-CTR (80 min). d) Z_H from operational ECCC radar (Strathmore, AB), 0.4 deg PPI. $Q_{i,tot}$ contours are 10^{-6}, 0.001, 0.1, ... g kg^{-1} (intended for illustration only).

3 Results of control simulations

3.1 Choice of analysis times

In order to reduce the quantity of analysis presented, specific times are chosen for each case for which the microphysical fields are examined. The times selected are during the mature, quasi-steady stages of the model storms and are representative of the hail growth at other times. Periods of the modeled storm evolution for the two cases are given in Fig. 4, which shows snapshots at various times for the column-maximum model equivalent reflectivity ($Z_{e,c}$) and ice mixing ratios ($Q_{i,tot}$) at the lowest model level, as well as the domain-maximum vertical motion. The simulation times of interest chosen are 60 and 80 min for the OK and AB cases, respectively. At these times, both storms are well developed and produce hail at the surface. In the figures discussed below, vertical cross sections along the dashed lines in Figs. 5c,6c are shown. The cross-section lines are chosen subjectively (but consistently for each run) by the following criteria: the lines cross through the point of maximum $Q_{i,tot}$ at the lowest model level (or the point of maximum $Z_{e,c}$ if the near-surface ice field is zero) and at prescribed meteorological angles of 335° for OK case and 115° for AB case, from the rear to the front of the storms. For the remainder of the paper, microphysical fields are examined at these times and locations. However, the microphysical sensitivities discussed below are general and occur at other times (with occasional minor differences).

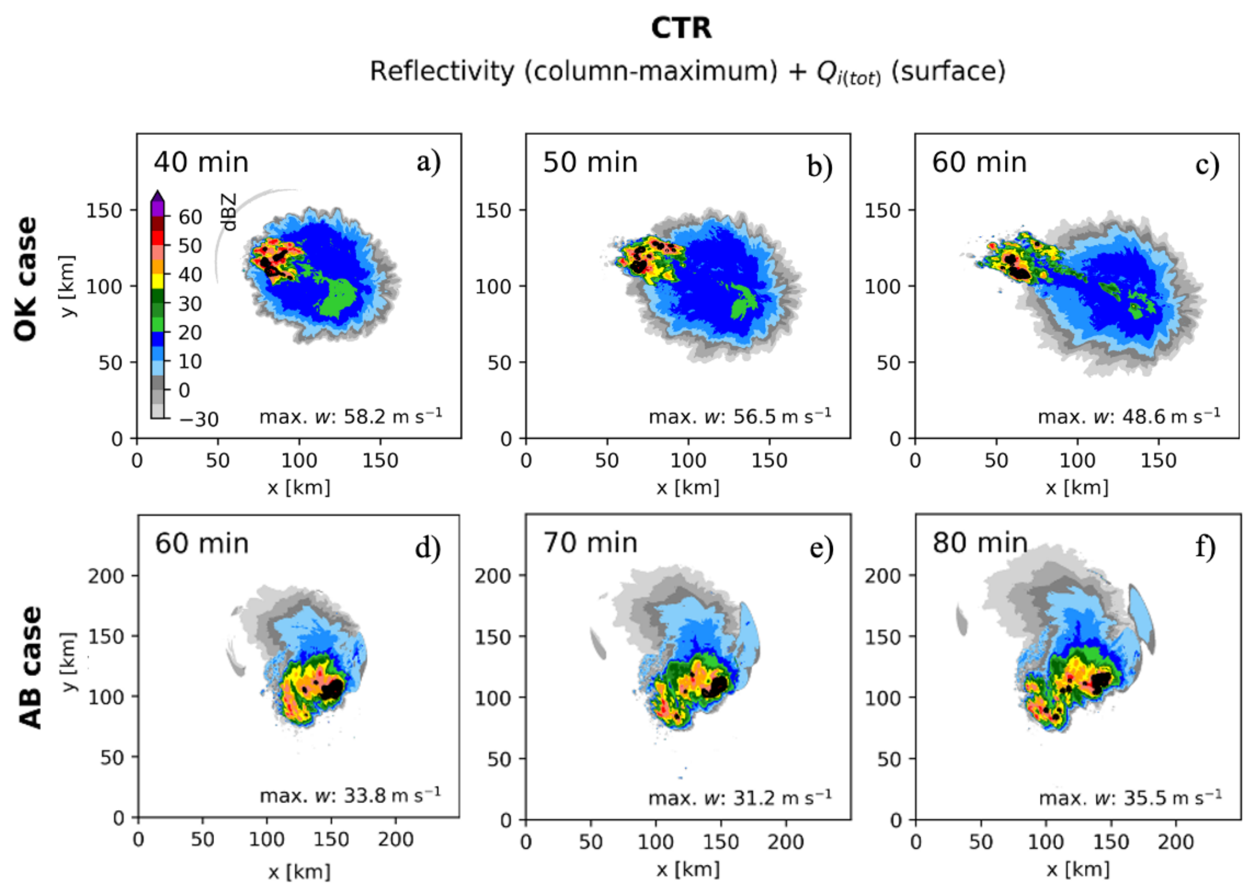

Figure 4. Column-maximum reflectivity ($Z_{e,c}$, shaded) and near-surface (lowest model level) ice mass mixing ratio ($Q_{i,tot}$, contours of 10^{-6}, 0.001, 0.1, ... g kg^{-1}) at 40, 50, and 60 min (OK-CTR, top) and at 60, 70, 80 min (AB-CTR, bottom). Domain-maximum vertical motion (max. w) is indicated numerically in each panel. (Note, the $Q_{i,tot}$ contours are intended only to illustrate the location of hail near the surface.)

3.2 Case 1: OK 2008

Results for the OK-CTR run at 60 min are summarized in Fig. 5. The left column shows vertical cross sections (see location in Fig. 5c) of the total ice, cloud water, and rain mass contents (Fig. 5a) and Z_e (Fig. 5b), the near-surface (first model level) Z_e and ice content (Fig. 5c) and the total and solid precipitation rates (Fig. 5d). The panels in the right column shows various fields related to ice: the total ice mass content (Q_i) (which includes the liquid portion, when relevant), number concentration (N_i), rime mass fraction (F_{rim}), liquid fraction (F_{liq}; not relevant for the CTR but plotted for consistency with subsequent figures), mass-weighed mean density (ρ_i), mass-weighted mean fall speed (V_m), mass-weighted mean diameter (D_m), and maximum hail size ($D_{h,max}$). Note, the mass and number fields are converted from mixing ratios to concentrations for the vertical cross-section plots.

Despite this run having only a single ice-phase category, overall distributions of the ice physical properties are consistent with what one would expect in a strong deep convective storm. Most of the ice is heavily rimed ($F_{rim} > 0.7$; Fig. 5g), even the ice falling out of the anvil, owing to it originating within the strong convective updraft, with copious amount of liquid water available for riming (Fig. 5a), before being lofted and transported horizontally. In the convective core the ice has high density (Fig. 5i), large sizes (Figs. 5k), and fast fall speeds (Fig. 5j). At high altitudes (e.g. z > 10 km) in the anvil, the ice is small (Fig. 5k) and dense (Fig. 5i), with evidence of gravitational size sorting in forward part of the anvil, and larger mean ice sizes and fall speeds at lower elevations (Figs. 5k,j). Note that frozen drops are initialized as rimed ice, in order to prescribe an initial bulk density as that of solid ice upon initiation. Technically this is not rime, but it allows the model to properly initiate and track the properties (density, shape). The maximum hail size, $D_{h,max}$, appears as the shaded regions in Fig. 5l. The largest sizes are constrained to a narrow shaft in the convective core, reaching the surface along the right flank (Figs. 5c,d), while smaller hail is lofted and ejected into the anvil, melting before reaching the surface. With the liquid-fraction shut off for the control run, the F_{liq} field (Fig. 5h) is not applicable (or could be considered zero by design).

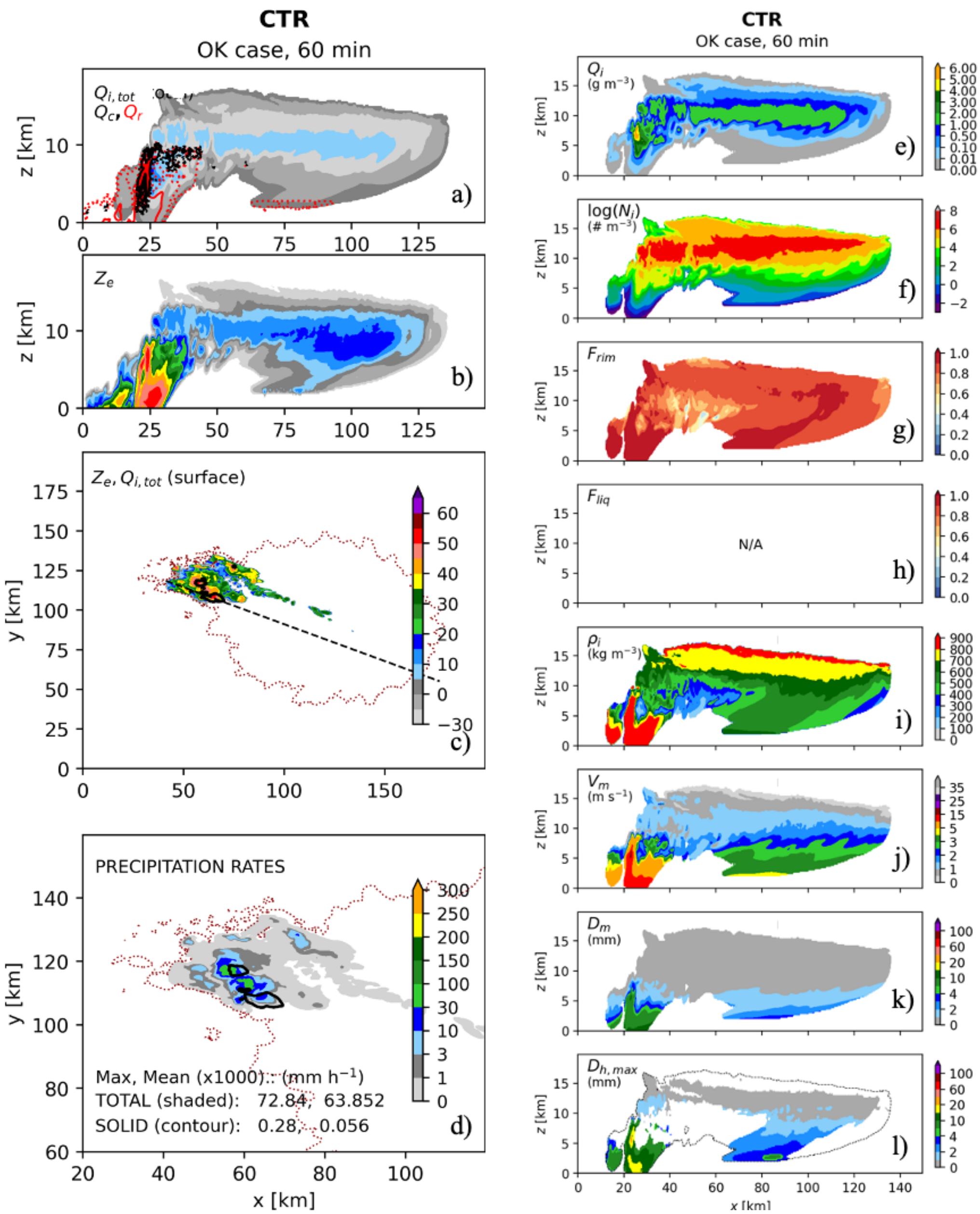

Figure 5. OK-CTR simulation at 60 min. a) Vertical cross-sections of Q_i (shading), Q_c (black contours) and Q_r (red contours), with shading boundaries and contours of 0.1, 1, 3, 5, and 10 g m^{-3}). b) Near-surface (lowest model level) Z_e (shading) and Q_i (contours; 10^{-6}, 0.1, and 1 g m^{-3}). c) Total (shaded) and solid (contours) surface precipitation rates (same shading boundaries/contours). Domain maximum and mean for each are indicated numerically. The right column has vertical cross sections of e) Q_i, f) N_i, g) F_{rim}, h) F_{liq}, i) ρ_i, j) V_m, k) D_m, and l) $D_{h,max}$. The line of the cross-sections is indicated in b). Note, all mass and number mixing ratios (quantity kg^{-1}) are converted to concentrations (quantity m^{-3}) for plotting. The dotted red contours in b) and c) are the 30 dBZ $Z_{e,c}$ isopleths. The dotted line in l) denotes the 10^{-12} g m^{-3} Q_i isopleth.

3.3 Case 2: AB 2022

The storm structure for the AB-CTR simulation (Figs. 4d-f, 6a,b) is notably different from the OK case (Figs. 4a-c, 5a,b), but the overall distributions of the ice physical properties are similar (Figs. 6e-l). There are some quantitative differences, such as lower values of F_{rim} (Fig. 6g) and ρ_i (Fig. 6i) further downstream in the anvil, probably due to weaker updraft strengths in the AB case (Fig. 4) and thus less dominance of ice from frozen drops transported from the convective core. However, the overall similarity of ice property distributions despite the different storm structures lends support to the generality of the sensitivity test results presented below.

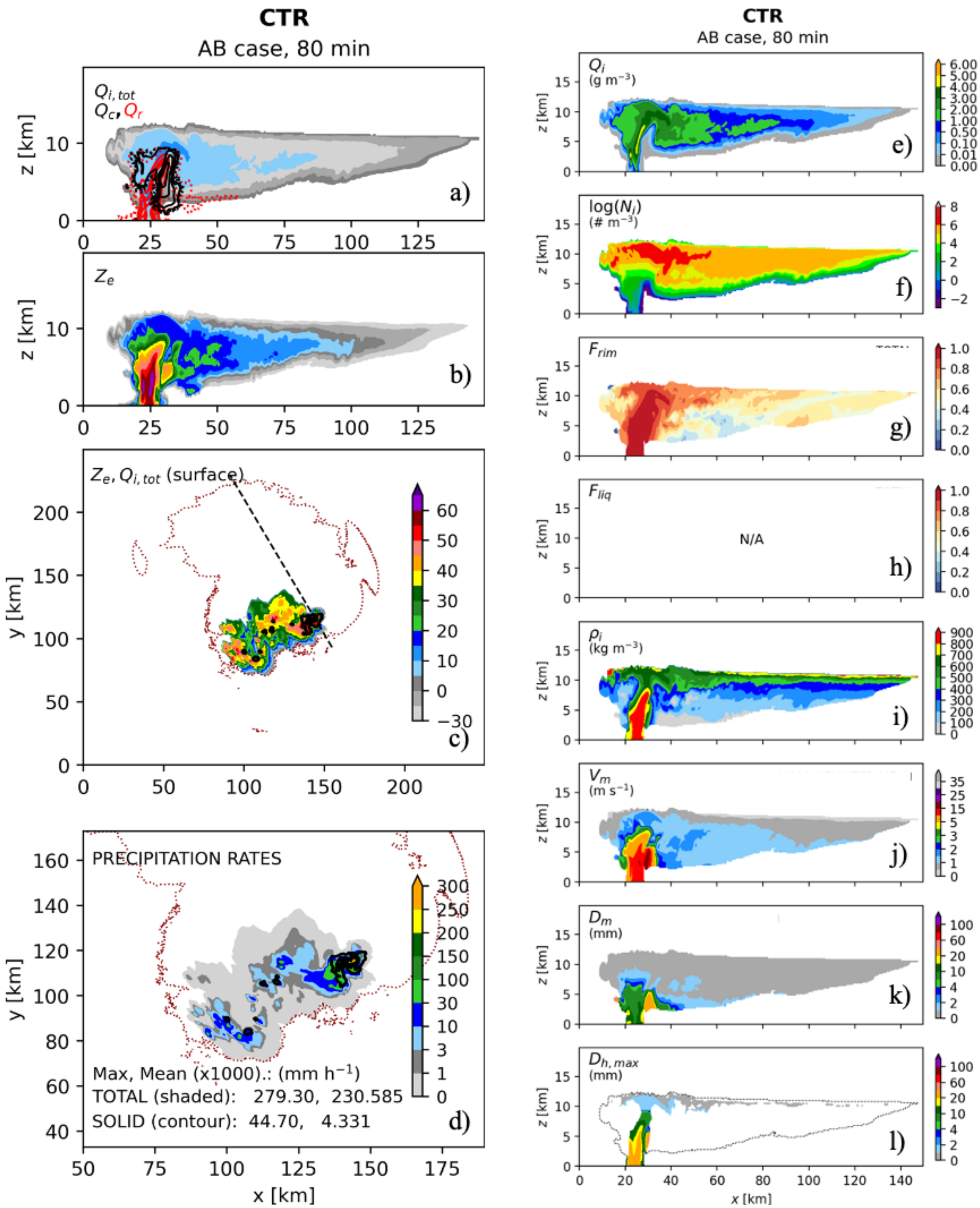

Figure 6. As in Fig. 5 but for AB-CTR simulation at 80 min.

4 Microphysics sensitivity tests

4.1 Impacts of liquid fraction

The impacts of the prognostic liquid fraction are examined here. The ice fields are summarized in Fig. 7 for OK-LF at 60 min in the left column (corresponding the right column of Fig. 5 for OK-CTR) and for AB-LF at 80 min in the right column (corresponding to the right column of Fig. 6 for AB-CTR). Most of the ice fields are quite similar to those of the corresponding CTR runs, but with some notable and important differences. The F_{liq} field is now defined and while it is zero for most locations with ice present, it increases to 1 with decreasing height as the ice melts (Figs. 7d,l). Although it is not apparent in Fig. 7, F_{liq} can also be non-zero in the hail growth zone if the ice is undergoing wet growth. Also, with the predicted liquid fraction the model reflectivity is more realistic in melting regions as a result of the bright band (not shown) being accounted for (Cholette et al., 2023). The important impact of the inclusion of liquid fraction pertaining to this study is that the quantity and size of ice/hail reaching the surface is notably reduced in both cases (Figs. 7a,g,h,i,o,p). This is consistent with reduced domain-maximum and domain-mean solid precipitation rates for OK-LF and AB-LF (Table 2).

This significant reduction of hail reaching the surface is due to differences in the way melted ice mass is treated with liquid fraction on and the closure assumptions pertaining to the ice number tendency during melding and shedding, all of which we believe increase the realism of these parameterized processes in P3. With liquid fraction off, melting in P3 is treated as follows: The amount of total ice mass that melts in one time step is computed, following the heat balance equation (see Morrison & Milbrandt, 2015 for details), and is assumed to be immediately and completely shed to rain. The $N_{i,tot}$-tendency due to melting is parameterized using the closure assumption of a constant mean-mass diameter D_{mm}, defined by

$$D_{mm} = \left(\frac{6}{\pi\rho_i}\cdot\frac{Q}{N}\right)^{1/3}, \qquad (2)$$

which is commonly used in multi-moment bulk schemes (e.g. Ziegler, 1985; Ferrier, 1994; Milbrandt & Yau, 2005b; Morrison et al., 2005; Mansell et al., 2010). In (2) and the equations below, the "*i,tot*" subscripts are excluded from $Q_{i,tot}$ and $N_{i,tot}$ for conciseness. Note that for a gamma size distribution, this is equivalent to assuming a constant slope (λ) and shape parameter (μ) for this process. With this assumption, the ratio $Q_{i,tot}/N_{i,tot}$ remains constant so $N_{i,tot}$ decreases proportionally to $Q_{i,tot}$ during melting, following

$$\left(\frac{dN}{dt}\right)_{MELT} = \frac{N}{Q}\cdot\left(\frac{dQ}{dt}\right)_{MELT}. \qquad (3)$$

where $(dQ/dt)_{MELT}$ is the melting rate of $Q_{i,tot}$. With liquid fraction on, the treatment of the melted ice mass in P3 is physically more realistic (see Cholette et al., 2019 for details). In a given time step during melting, a portion of the solid mass, which is $Q_{i,tot}$ - $Q_{i,liq}$ (i.e. deposition plus rime mass), melts to liquid. Small ice particles are assumed to melt completely in the time step and thus the mass goes directly to rain (Q_r), with $N_{i,tot}$ decreasing as per (3) (for this portion of the melting only). The rest of the melted ice mass, however, is converted from solid to liquid but remains within the mixed-phase particles ($Q_{i,rim}$ decreases, $Q_{i,liq}$ increases, and $Q_{i,tot}$ remains the same), increasing the liquid fraction locally and with no change to $N_{i,tot}$. Shedding of liquid on mixed-phase particles is then calculated explicitly (see Cholette et al., 2019, 2023) and depends on the rime mass fraction, where at the extremes unrimed ice does not shed whereas fully-rimed ice sheds at the maximum rate. During shedding, $N_{i,tot}$ does not change while the rain mass and number increase. As a result, with liquid fraction on the melting of heavily rimed ice combined with shedding tends to result in a decrease in the mean ice size, as per (2).

For unrimed or lightly-rimed ice, the differences in mass changes during melting and the impacts of this are significant since with liquid fraction on the melted mass remains in mixed-phase particles, increasing their fall speed towards that of rain until the ice melts completely. For heavily-rimed ice, although there is a temporary transfer of most of the melted mass to liquid within mixed-phase particles, most of this mass is quickly shed; thus, the mass transfer from solid ice to rain is similar to that with liquid fraction off. However, the difference in the treatment of $N_{i,tot}$ during melting/shedding results in a much different change in D_{mm}, with the size decreasing much faster with liquid fraction on. This results in slower fall speeds, greater total surface area (since a given mass is distributed over more particles), and thus a faster mass melting rate – and ultimately melting hail is more likely to completely melt before reaching the surface. Therefore, with the exception of the change in $N_{i,tot}$ that can occur for the small melted fraction that goes directly to rain, for the melting that is first retained in the liquid portion of the mixed-phase particles and then shed, $N_{i,tot}$ remains constant.

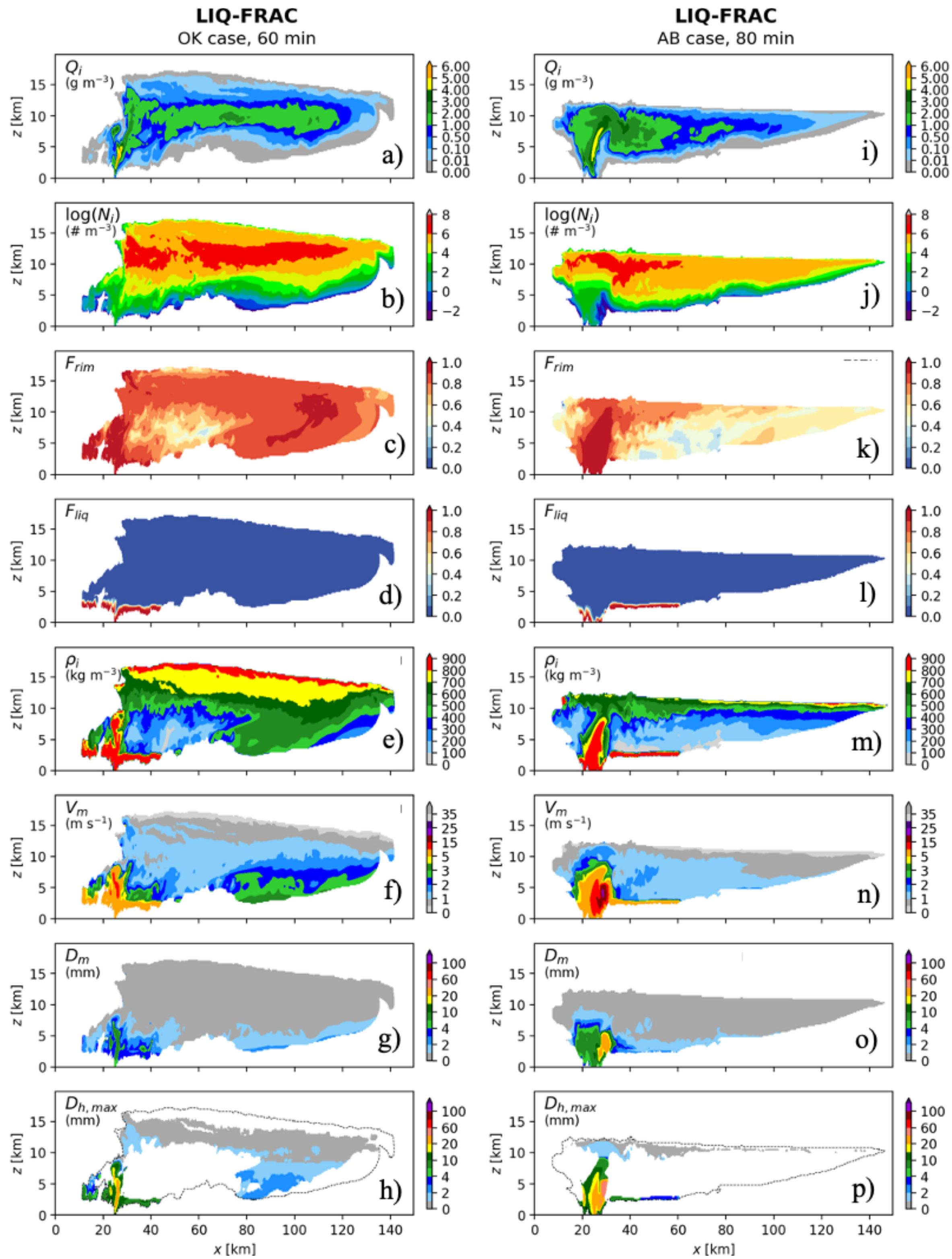

Figure 7. Bulk ice fields/properties for OK-LF (at 60 min, left) and AB-LF (80 min, right). The panels in each column correspond to those in the right column in Fig. 5.

Table 2. Total and solid surface precipitation rates at 60 min (OK case) and 80 min (AB case). Units are in mm h^{-1} for domain-maximum and 0.001 mm h^{-1} for domain-mean values.

Run name	**Total (max)**	**Total (mean)**	**Solid (max)**	**Solid (mean)**
OK-CTR	102.51	59.085	1.28	0.056
OK-LF	76.52	62.082	0.00	0.000
OK-CTR-MOD	94.04	100.528	0.00	0.000
OK-LF-MOD	134.37	67.362	2.04	0.087
OK-LF-2CAT	103.44	95.499	0.01	0.000
OK-LF-3CAT	128.85	58.073	2.20	0.055
OK-LF-4CAT	53.94	62.703	0.23	0.005
AB-CTR	279.30	230.585	44.70	4.331
AB-LF	242.51	241.034	18.84	1.310
AB-LF-2CAT	313.78	297.526	139.32	7.814
AB-LF-3CAT	268.53	291.970	155.61	19.016
AB-LF-4CAT	234.70	302.090	84.38	6.181

To illustrate that the differences described above are indeed responsible for the reduced hail at the surface in the OK-LF and AB-LF simulations with liquid fraction on, two sensitivity tests were run (for the OK case only). For the first test (OK-CTR-MOD), the code in the OK-CTR configuration was modified such that $(dN/dt)_{MELT}$ is set to zero, similar to the overall effect with liquid fraction on in OK-LF (except for the portion of small ice melting directly to rain). In the second test (OK-LF-MOD), the OK-LF configuration was modified such that $(dN/dt)_{MELT}$ is computed by (3) following the closure assumption for melting in OK-CTR, with $(dN/dt)_{SHED}$ set to zero since it is implicitly included in melting. The impacts on ice mass and mean sizes near the surface are shown in Fig. 8 (with fields from the unmodified OK-CTR and OK-LF also shown in Figs. 5 and 7, repeated to facilitate comparison). The OK-CTR-MOD run (Fig. 8d,e,f) is now similar to the OK-LF run (Fig. 8g,h,i), with no ice mass reaching the surface. Both D_m and $D_{h,max}$ are reduced, and the solid precipitation reaching the surface is now zero (Table 2). Conversely, OK-LF-MOD (Fig. 8j,k,l) is similar to OK-CTR (Fig. 8a,b,c), with ice/hail reaching the surface, increased particle sizes, and similar solid precipitation rates. Clearly, therefore, the differences in the closure assumptions for the changes in $N_{i,tot}$ during melting/shedding are largely responsible for the notable reduction of hail at the surface with the liquid fraction on configuration. The results for the same set of tests are qualitatively similar for the AB case (not shown).

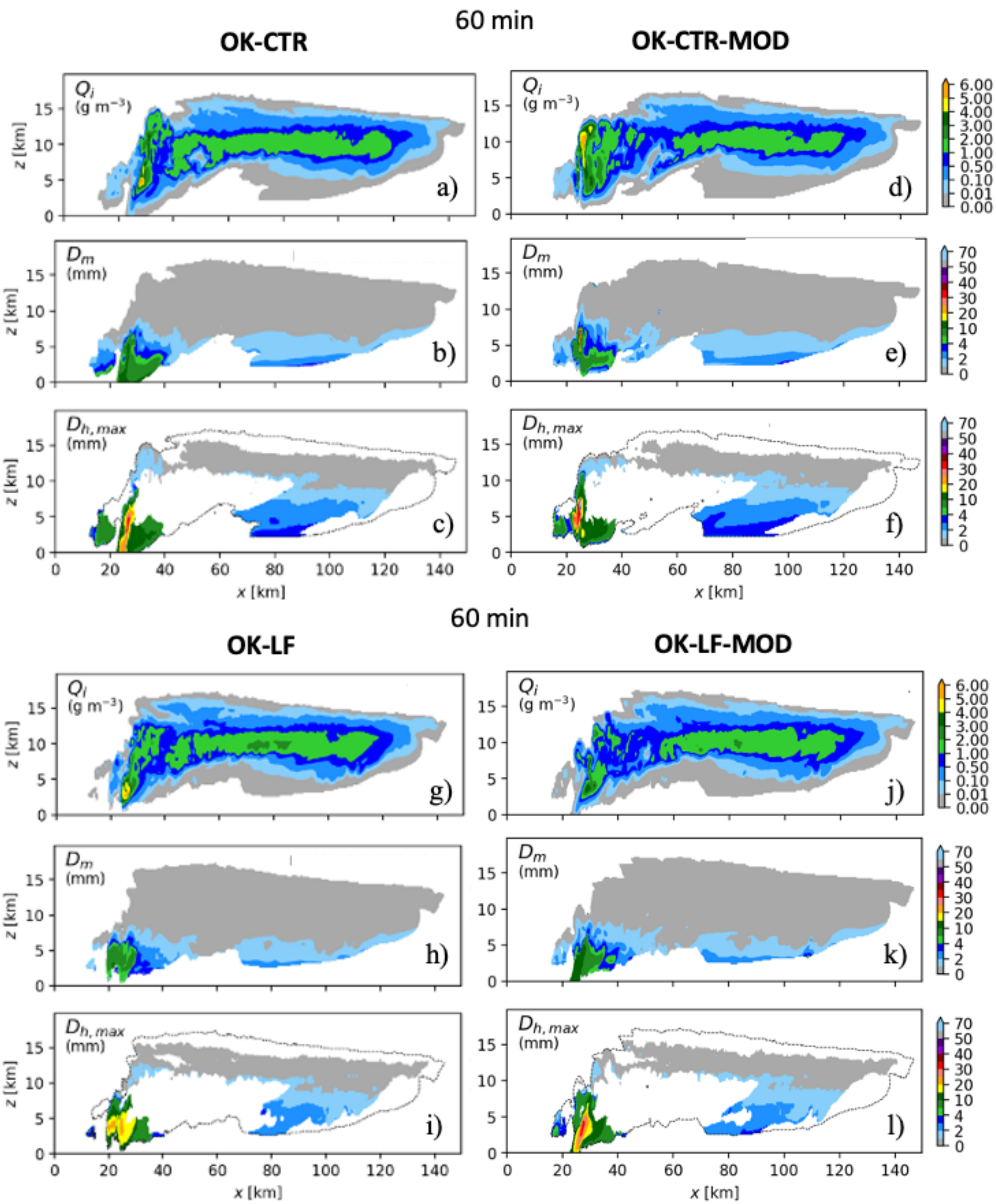

Figure 8. Vertical cross-sections of Q_i, D_m, and $D_{h,max}$ for OK case (at 60 min) for OK-CTR [top left; a), b), and c)], OK-CTR-MOD [top right; d), e), and f)], OK-LF [bottom left; g), h), and i)], and OK-LF-MOD [bottom right; j), k), and l)].

To illustrate further the differences in melting between these configurations, process rates related to melting/shedding for OK-LF are shown in Fig. 9. Here we partition melting into the portion of frozen ice mass that melts directly to rain (MELT1) and the portion that transfers frozen mass to liquid mass in the mixed-phase particle (MELT2). Figure 9a,b shows $(dQ/dt)_{MELT1}$ and $(dN/dt)_{MELT1}$, respectively. The mean particle size due this sub-process remains constant. Figure 9c shows $(dQ/dt)_{MELT2}$, which does not result in any change in $Q_{i,tot}$ (only a transfer from ice to liquid that remains on the particle), with the mass loss rate due to shedding given by $(dQ/dt)_{SHED}$ (Fig. 9d). The resulting rate of change of D_{mm} due to the combined melting and shedding, $(dD/dt)_{MELT+SHED}$, is given by

$$\left(\frac{dD}{dt}\right)_{MELT+SHED} = \frac{1}{3}\left(\frac{\pi}{6}\rho_i\right)^{-\frac{2}{3}} \cdot \left[Q^{-\frac{2}{3}}N^{-\frac{1}{3}}\left(\left(\frac{dQ}{dt}\right)_{MELT1} + \left(\frac{dQ}{dt}\right)_{SHED}\right) - Q^{-\frac{1}{3}}N^{-\frac{4}{3}}\left(\frac{dN}{dt}\right)_{MELT1}\right], \quad (4)$$

and is shown in Fig. 9e. Clearly the mean size of hail that melts and sheds in the convective cores ($x \sim 25$ km) decreases with the liquid fraction configuration. Note, in computing (4) (which is only diagnostic, for Fig. 9e) ρ_i is held constant for simplicity, so in fact (4) underestimates the rate of decrease in mean particle size. This is because for MELT2, although there is no change in total mass or number, frozen mass is transferred to liquid ($Q_{i,liq}$) which increases the mean particle density, thereby decreasing the mean size as per (2).

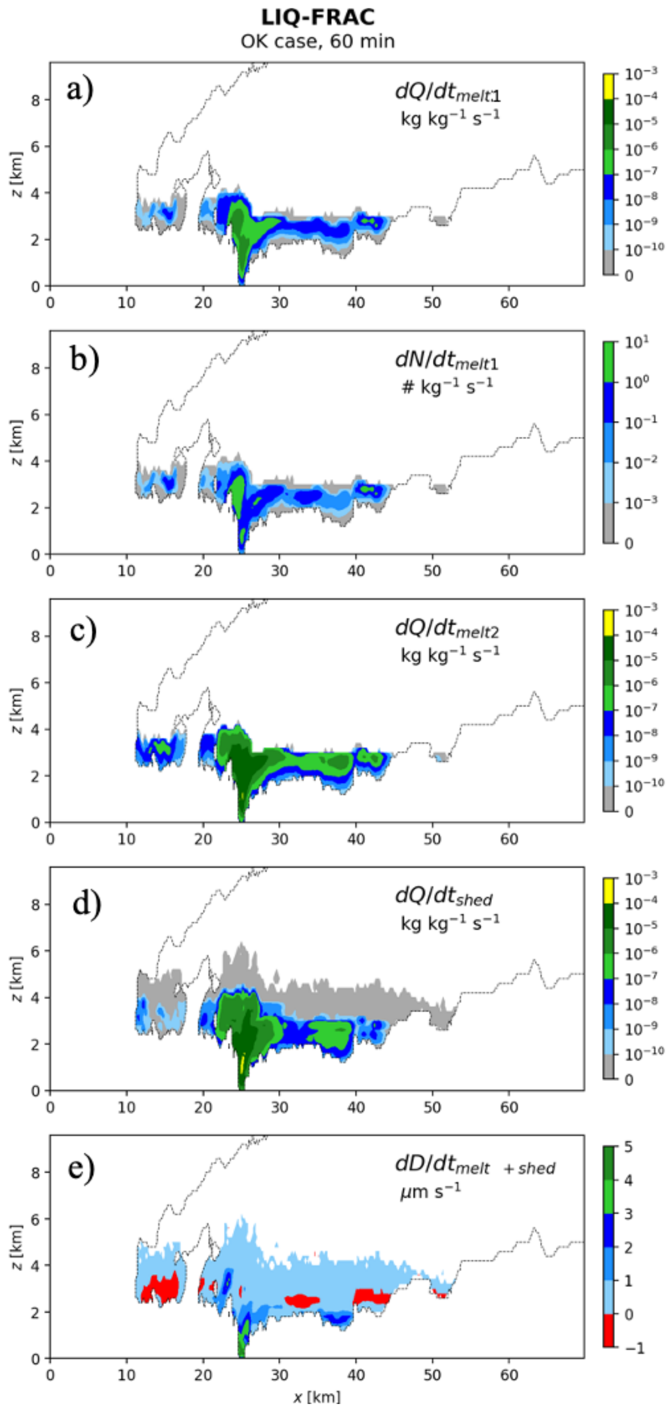

Figure 9. Process rates related to melting and shedding for OK-LF (at 60 min): a) and b) $Q_{i,tot}$ and $N_{i,tot}$ tendencies, respectively, due to complete melting (to rain) of small particles (MELT1); c) Tendency for mass transfer from solid to liquid within mixed-phase particles due to melting (MELT2); d) $Q_{i,tot}$ tendency due to shedding; e) D_{mm} tendency due to combination of melting to rain and shedding calculated from (4). See main text for details. Positive values denote decreases.

If we believe that the LF configuration indeed allows for a more realistic representation of melting and shedding, and also for representing complex mixed-phase winter precipitation (Cholette et al., 2019, 2024), a way to improve this in the liquid fraction-off configuration may simply be to replace the constant D_{mm} closure assumption for melting with the one tested in OK-CTR-MOD, at least for large values of F_{rim}. This may be considered for future versions of P3 since there is some computational cost associated with LF configuration (due to the additional prognostic variable, $Q_{i,liq}$). Similarly, the $(dN/dt)_{MELT} = 0$ approach may be a simple improvement in traditional bulk schemes for the graupel and hail categories that do not include prognostic liquid fraction. Note that an alternative approach to mitigating the assumption of (3) was explored by Mansell et al. (2020), guided by detailed bin scheme calculations of hail melting. It should also be noted that Loftus et al. (2014) predicted the liquid fraction (via prognostic heat content) for hail.

Shedding also happens during wet growth which can, in principle, be modeled more realistically with the predicted liquid fraction. With liquid fraction off, the shedding rate (mass) is computed as the dry growth rate (i.e. the total accretion rate of liquid water) minus the wet growth rate, computed from a heat balance equation, based on the Shuman-Ludlam limit (Young, 1993). With liquid fraction on, this difference in unfrozen collected mass remains as liquid on the particles (F_{liq} increases); shedding of a portion of this liquid is then computed separately. This is depicted in Fig. 1. Thus, wet hail can be represented and the liquid remaining can re-freeze onto the existing ice once wet growth stops, so in principle hail can acquire larger mass contents and sizes. This is a potentially interesting (and aesthetically curious) aspect of the liquid-fraction configuration of P3 and it will be examined in a future study. However, the capacity to model wet hail growth is probably much less important than the improved capacity to model the melting/shedding of ice in general, including for the simulation of hail at the surface.

4.2 Impacts of the number of ice categories

As illustrated in section 3.1, even with a single ice category P3 can simulate a wide and continuous range of ice particle physical properties, and hence a wide range of frozen hydrometeor types. With the liquid fraction configuration, mixed-phase particles can also be represented and the associated microphysical processes better modeled. The limitation, however, is that only a single set of properties – and hence one dominant particle type – can be present at a given point in time and space. The multi-category configuration of P3 removes this limitation and allows for multiple sets of properties, and thus multiple modes, to coexist and to evolve independently. The details of ice initiation into a given category and the merging of categories with similar properties are explained in Milbrandt & Morrison (2016).

To examine the impact of multiple categories on the simulation of hail, a second set of sensitivity runs for each case was conducted, increasing the number of categories (*nCat*) from 1 to 4 (incrementally). All of these runs were with liquid fraction on, thus the control runs for this analysis become OK-LF and AB-LF. The fields for each of the ice categories in OK-LF-2CAT are shown in Fig. 10. At any given location, the physical properties are quite often different between the two categories, and are also different from the single-category run, OK-LF (Fig. 7). With the 3-category run (OK-LF-3CAT, Fig. 11), not only is the ice in category 3 (Fig. 11, right column) different from the other two, but the ice in categories 1 and 2 of OK-LF-3CAT (Fig. 11, left and middle columns) are different from those of OK-LF-2CAT (Fig. 10). For example, the mean particle sizes are much larger (> 10 mm) in category 2 for the ice at lower levels in the anvil (Fig. 111o) than those of category 2 in OK-LF-3CAT (Fig. 10o), with D_m values < 4 mm. These differences emphasize that a given ice category in the multi-category configuration is not predisposed to represent a particular mode/type of ice; each category is equally continuous and variable. Also, a given category is not predisposed to a particular set of dominant properties, though for both OK-LF-2CAT and OK-LF-3CAT most of the ice mass resides in category 1 (top rows of Figs. 10, 11). The ice fields for each category of the OK-LF-4CAT run (not shown) support this further. These results are consistent with the simulations for the AB cases, discussed below.

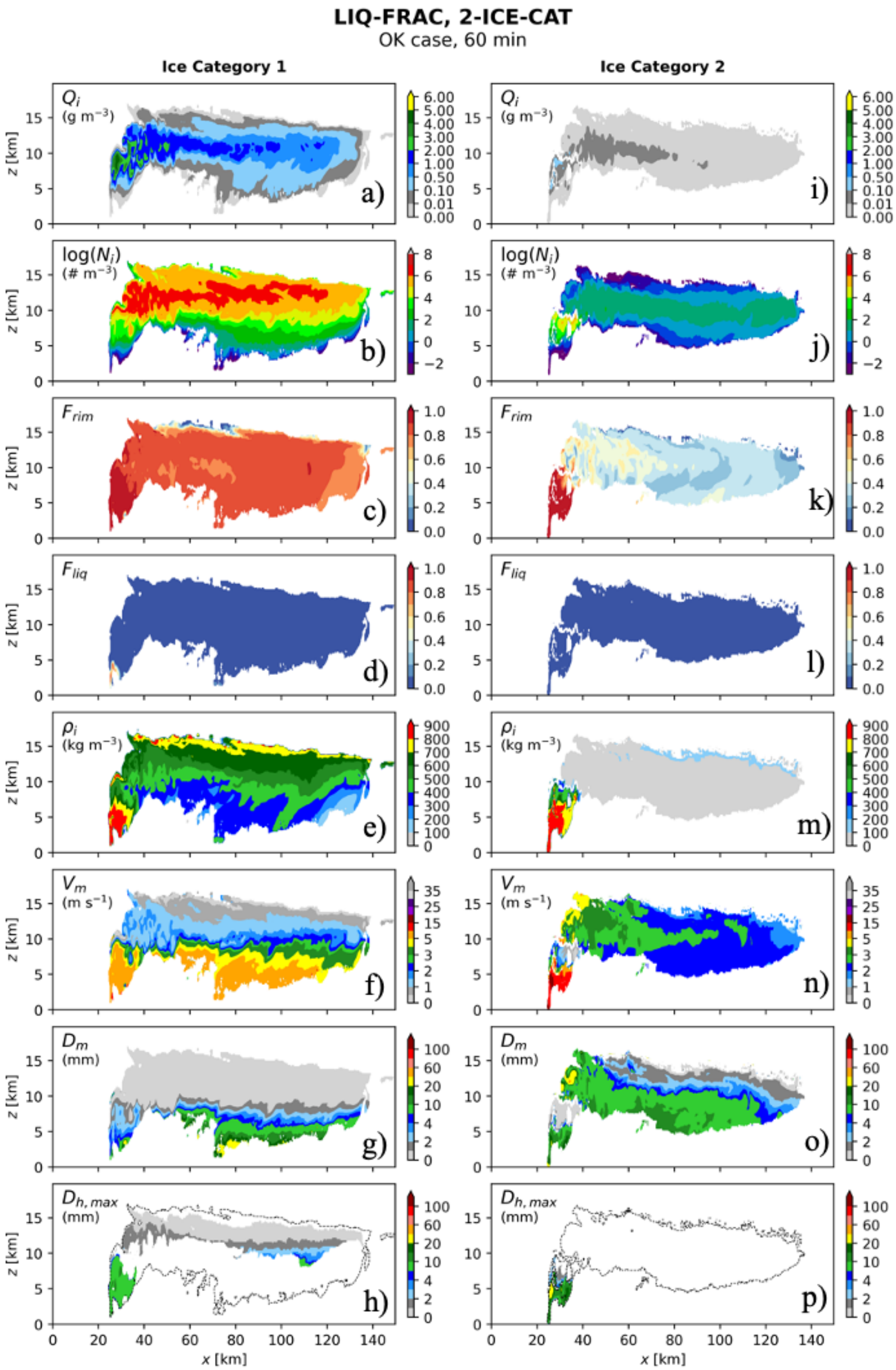

Figure 10. As in the right column of Fig. 5 but for ice category 1 (left) and category 2 (right) for OK-LF-2CAT (60 min).

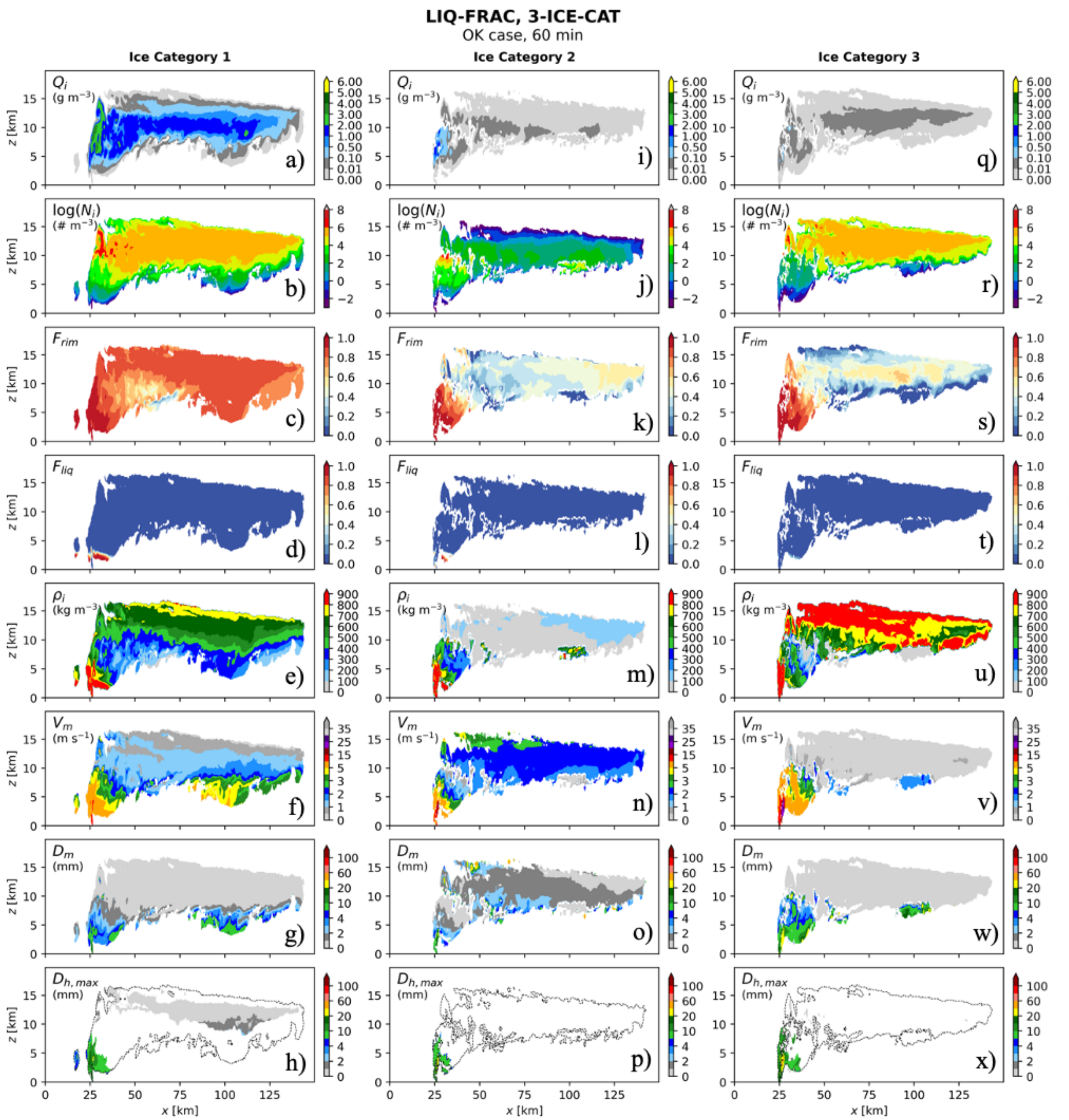

Figure 11. As in the right column of Fig. 5 but for ice category 1 (left), category 2 (middle), and category 3 (right) for OK-LF-3CAT (60 min).

Figure 12 summarizes the "bulk" ice fields for all categories for the OK-LF-2CAT, OK-LF-3CAT, and OK-LF-4CAT simulations. For the total mass and number this is the sum of $Q_{i,tot}(i)$ and $N_{i,tot}(i)$ over all i in 1 to $nCat$ (converted to mass and number concentrations, Q_i and N_i); the "total" F_{rim} and F_{liq} are computed from the appropriate sums of the ice fields; ρ_i, V_m, and D_m are mass-weighted averages of each category; and D_{h_max} is the maximum value amongst the categories. These bulk fields can be compared directly to the 1-category run, OK-LF (Fig. 7). For the AB case, the corresponding results for the multi-category simulations are shown in Figs. 13-15.

For both cases, despite the internal variability within the individual categories exhibited in Figs. 8, 9, 13, 14 (and also for the 4-category runs, not shown), the bulk fields are broadly similar for all of the simulations, as well as to those of the 1-category runs (Fig. 7). However, there are some important differences with respect to the simulation of hail with variation in the number of ice categories. In general, the hail quantity and size increase as the number of ice categories is increased. This is evident from the hail mass reaching the surface around the convective core ($x \sim$ 25 km, top rows of Figs. 7, 12, 15), the mean particle sizes D_m (second last rows), the maximum hail sizes $D_{h,max}$ (last rows), as well as the domain-mean and domain-maximum solid precipitation rates at those times (Table 2). For the 4-category runs the solid precipitation rates are, on the other hand, lower (than the 3-category runs) at those particular times; however, there is still abundant large hail reaching the surface (e.g. Figs. 12q,x, 15q,x), notably more than the 1- and 2-category runs (and the 3-category run for the AB case). Note, although periods of hail can be intermittent and the results shown above are for individual cross-sections for snapshots in time, these results were similar at other times during the simulations (not shown), and are similar for both cases. Thus, this impact on hail with multiple ice categories in P3 can be considered general.

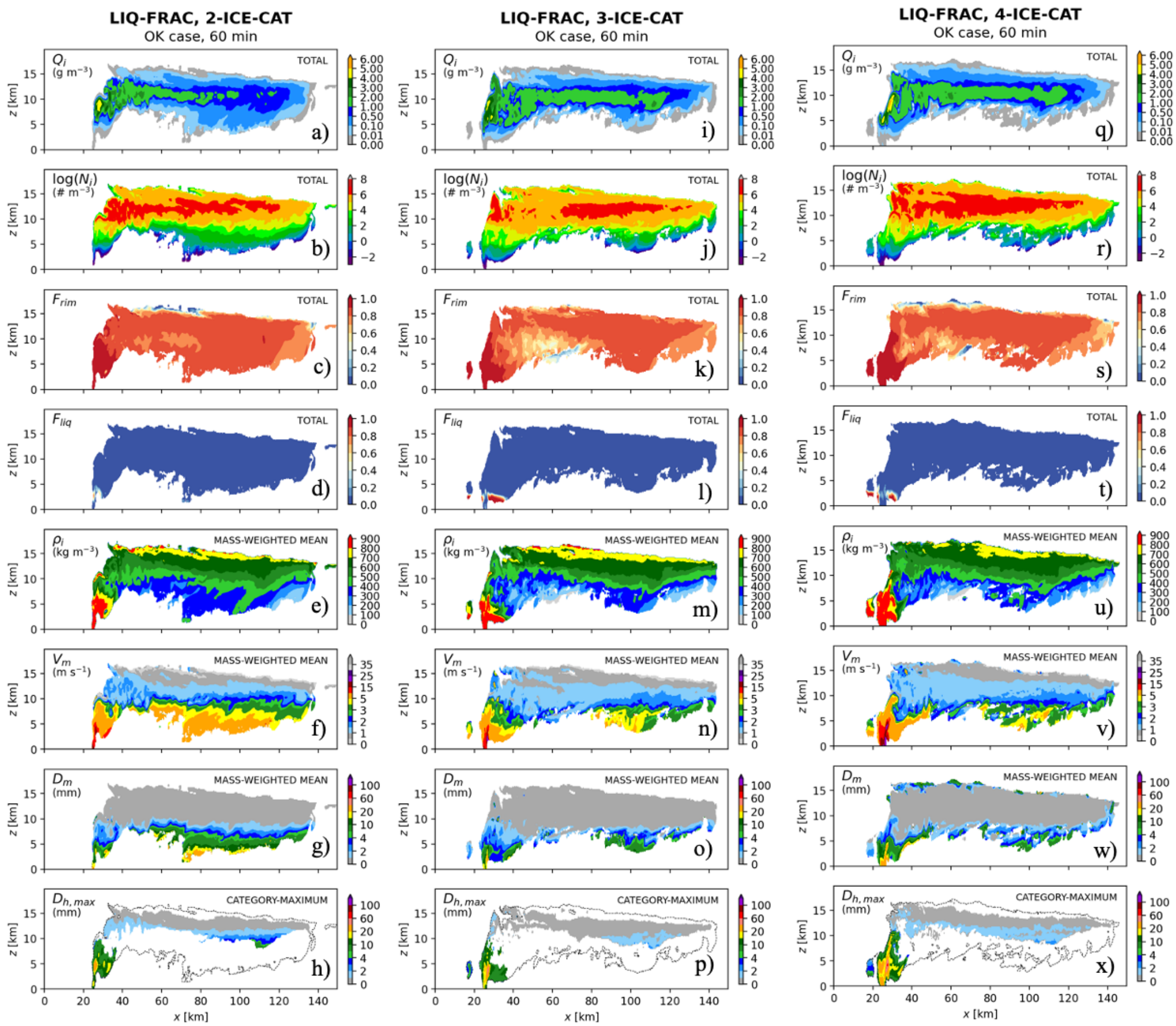

Figure 12. Bulk ice properties from OK-LF-2CAT (left), OK-LF-3CAT (middle), and OK-LF-4CAT (right) (60 min). The panels in each column are similar to those in the right column of Fig. 5, but are the sum (for Q_i and N_i) across all categories, the values computed from the appropriate sums (for F_{rim} and F_{liq}), or the mass-weighted values (for ρ_i, V_m, D_m, and $D_{h,max}$) considering each ice category.

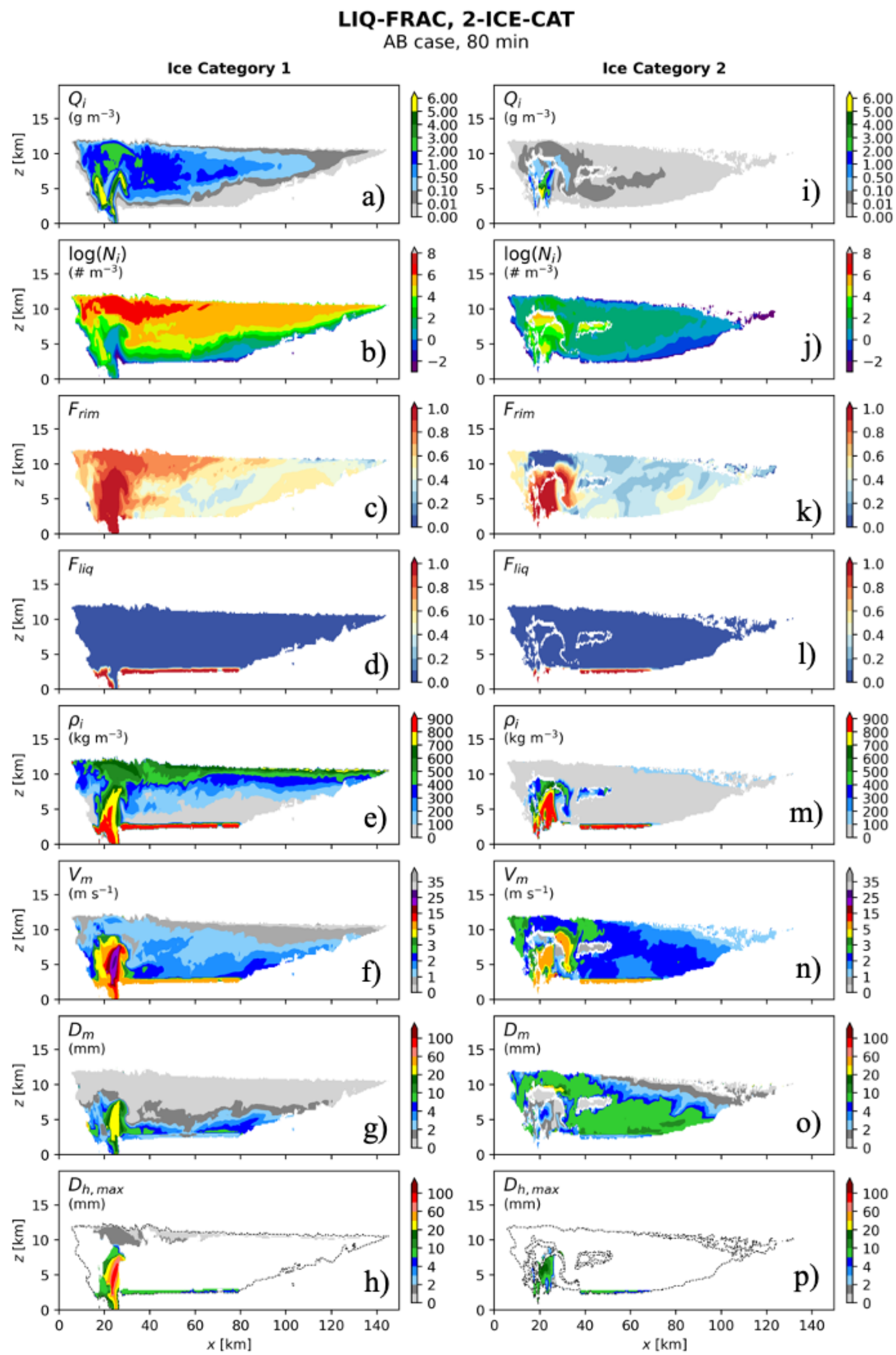

Figure 13. As in Fig. 10 but for AB-LF-2CAT (80 min).

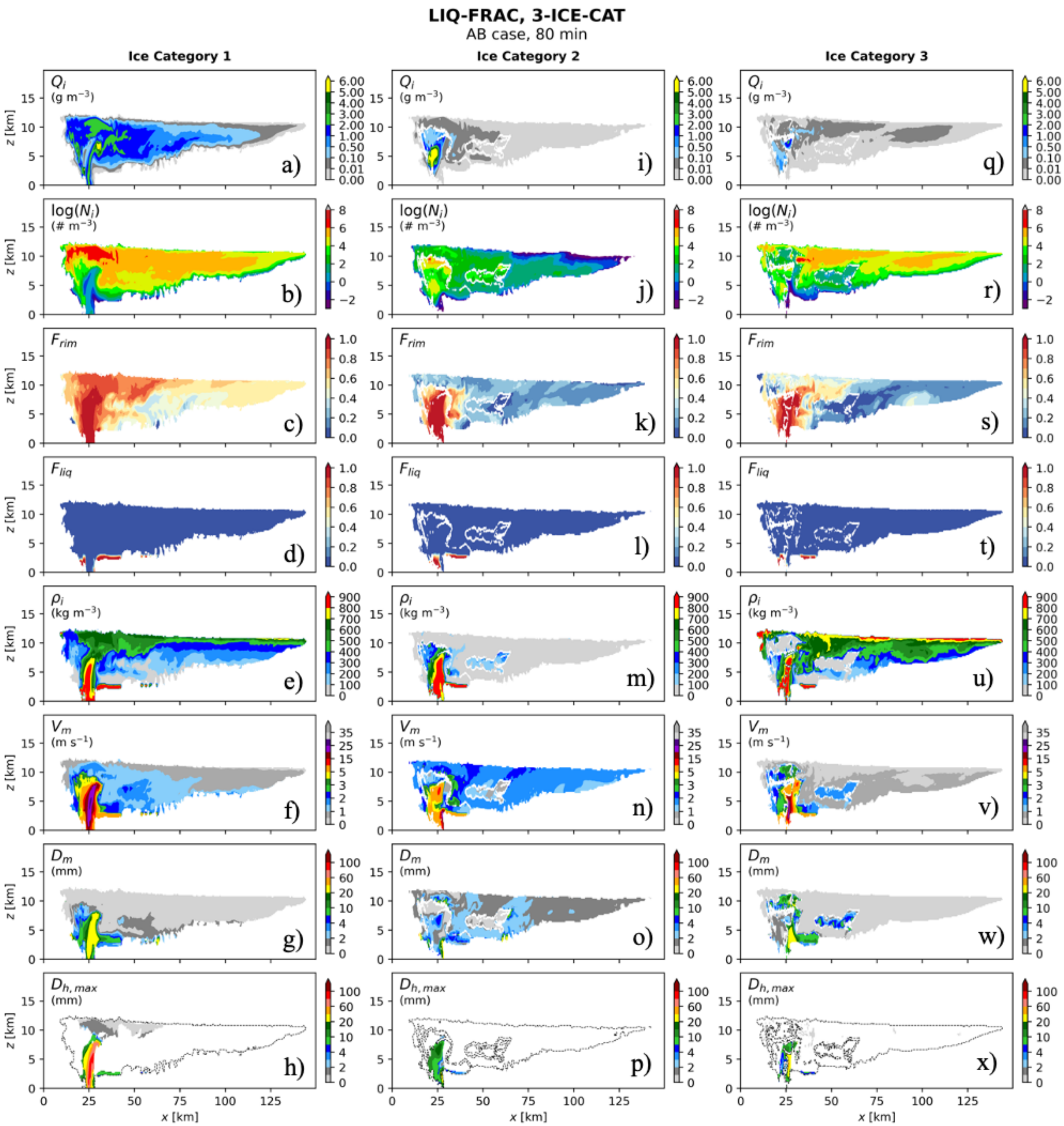

Figure 14. As in Fig. 11 but for AB-LF-3CAT (80 min).

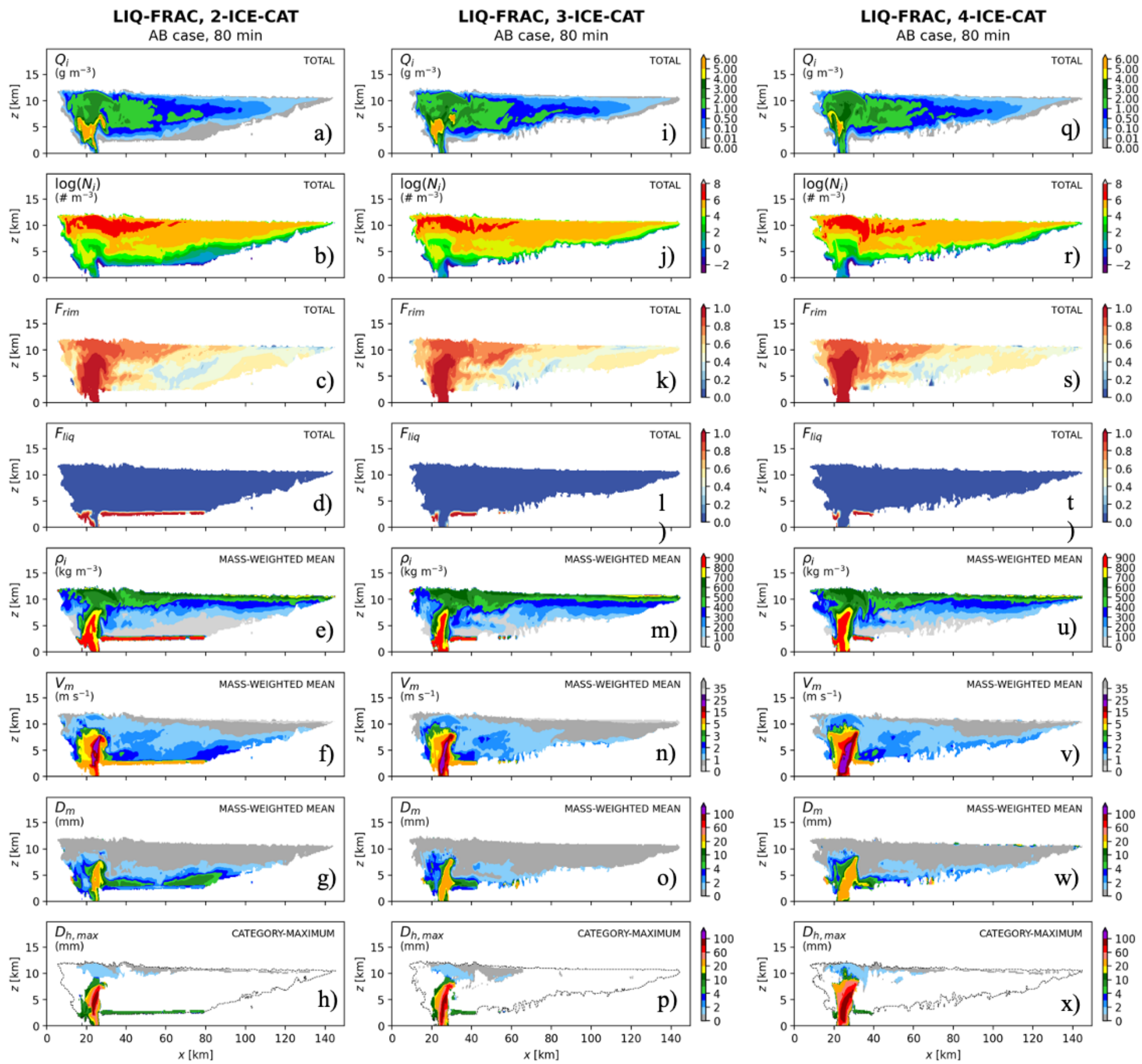

Figure 15. As in Fig. 12 but for AB-LF-2CAT (left), AB-LF-3CAT (middle), and AB-LF-4CAT (right) (at 80 min).

The use of multiple ice categories increases the hail amount and sizes, which presumably is an increase in the realism of the simulations because with the capacity to represent two or more sets of physical properties in the same location the problem of property dilution is reduced. Property dilution occurs when, for example two modes (i.e. sets of properties) that would otherwise exist independently are represented with a single distribution; the result is a kind of averaging of the properties, hence “dilution”. For hail, this dilution can be detrimental to subsequent growth since the particle properties such as fall speed and cross-sectional area are important in determining the collection rate of liquid water. This is illustrated in Fig. 16 which is a zoomed-in view of some fields of bulk ice properties that impact hail growth rates for the 1-category (AB-LF) and 2-category (AB-LF-2CAT) simulations. Note the properties in the hail core region, around 5 km AGL and $x \sim 30$ km: for ice category 1 in AB-LF-2CAT, V_m is greater than 20 m s^{-1} (Fig. 16d) and D_m is larger than 20 mm (Fig. 16e), whereas for category 2 in the same location V_m is 5-10 m s^{-1} (Fig. 16g) and D_m is smaller than 3 mm (Fig. 16h). With a peak updraft speed of around 35 m s^{-1} (assuming a similar speed as AB-CTR at that time; Fig. 4f) this means that the particles in category 1 can reside longer in the hail growth zone and grow to larger sizes, which is evident with the much larger values of $D_{h,max}$ (Fig. 16f). For the 1-category run (AB-LF), the property values in that region are in between those of the two categories in AB-LF-2CAT and the maximum hail sizes at the surface are indeed smaller in the hail shaft region (Fig. 16c). Note, the properties in this region in AB-LF cannot be interpreted as the literal average of the properties in categories 1 and 2 of AB-LF-2CAT since they are different simulations. However, the comparison in Fig. 16 is useful to illustrate how multiple ice categories in P3 reduce property dilution and allow for more realistic growth of larger hail, and ultimately to more hailfall at the surface and with larger sizes.

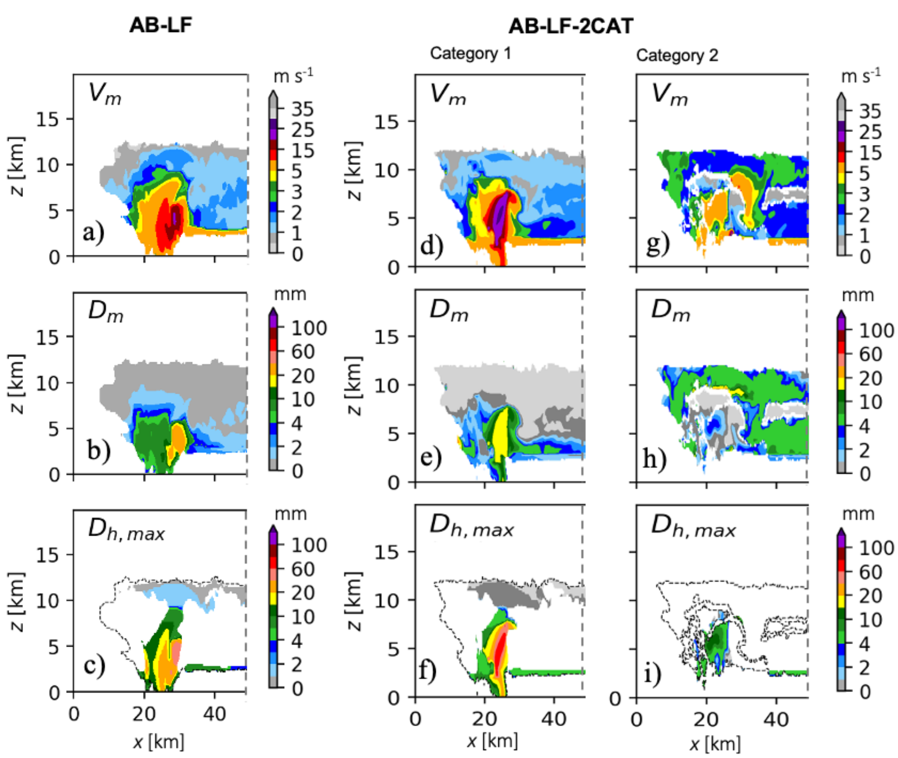

Figure 16. Zoom-in of V_m (top), D_m (middle), and $D_{h,max}$ (bottom) for AB-LF (left) and ice categories 1 (middle) and 2 (right) for AB-LF-2CAT. (Reproduced from Figs. 7 and 13.)

5 Discussion

Although the simulations presented are quasi-idealized and without a rigorous "verification" against observations, and evaluation against a numerical "truth" simulation is impossible since no perfect microphysics scheme exists, it is reasonable to believe that the aspects of P3 explored above improve the overall realism in representing ice-phase and mixed-phase microphysics in general, including the modeling of hail. It may appear initially that liquid fraction is detrimental to simulating hail, given that, for example, OK-LF has no hail but OK-CTR does, as did the observed storm. However, one must remember that the results from any numerical simulation come from the sum of all components of the model and this can include compensating errors. For melting of ice, the physics is better represented by a scheme that can model mixed-phase particles and the gradual transfer of ice to liquid within the particles followed by shedding. So, while the predicted liquid fraction appears to worsen the simulation of hail, at least for the OK case, the simulation of the specific processes of melting and shedding most likely improved. In the single category CTR configuration, the compensating error (or limitation) is the representation of all ice in the updraft with a single set of physical properties at a given point in time and space (i.e., in a grid cell), including fall speed, which has the effect of limiting hail growth to large sizes. Since all ice categories in multicategory configurations in P3 are subject to the identical parameterized processes and since additional categories reduce property dilution and hence improve the representation of the overall total ice, simulations should – in principle – always improve with an increased number of categories.

The multi-category P3 configuration could be optimized, or at least improved, such that there is a higher degree of "spread" of the properties amongst the various categories and thus a greater mitigation of property dilution. In the multi-category configuration, newly initiated ice (by primary nucleation, drop/droplet freezing, or secondary ice production) and ice in existing categories are compared in terms of overall similarity of bulk properties. New ice is added to the category that is most similar in terms of particle properties, or to a category containing no ice if one is available. At the end of the time step, ice categories that are evaluated as being similar are merged into a single category in order to free up the category for new ice. In the current configuration, D_m is used as the proxy to evaluate overall similarity, where two populations of ice (two categories or new ice and a given category) are deemed to be similar if their difference in D_m is below a certain threshold (which is a prescribed parameter but is a decreasing function of the number of categories; see Milbrandt & Morrison, 2016). The optimal similarity condition depends on the number of ice categories used and on the type of weather being simulated, since the ultimately purpose of multiple categories is to maximize the reduction of property dilution. In order to simulate large hail optimally with multiple categories, one needs to be able to distinguish ice that represents small graupel from ice that represents large hail. In this regard, the use of D_m as a proxy for similarity is reasonable (as per the discussion above pertaining to Fig. 16), though it could likely be improved. In contrast, for a large-scale baroclinic system with relatively little riming, the ability to distinguish graupel from hail is unnecessary so optimization likely means maximizing the ability to separate unrimed ice of different size ranges and/or unrimed ice from rimed ice of similar mean sizes. The proxy for overall property similarity based on D_m means that a population of high-density, heavily-rimed ice could be classified (by the current algorithm) as being similar to a population of low-density, unrimed ice with a similar mean size and hence could be merged into a single category, thereby violating the principle of minimizing property dilution. In a future study, we will explore and attempt to design an improved multi-ice-category configuration of P3, optimized for a wide range of category numbers and types of weather. This will likely use V_m as a similarity proxy and with three categories to ensure the separation of unrimed ice, graupel, and hail.

Despite potential weaknesses in the current configuration, it is important to recognize that a suboptimal multi-ice-category configuration of P3 is still a conceptual and effective improvement compared to the 1-category configuration (though it could, in principle, lead to a worse solution due to compensating model errors), but one with less improvement than is possible. This is simply a logical deduction from the fact that all ice categories are treated with identical parameterized process and the premise that the separation of ice into "free" categories in P3 reduces property dilution and improves representation of ice hydrometeors. There are two extremes in which a multi-category configuration would be least optimal. In the first, if the similarity condition is such that all newly-formed ice goes into the first available category such that there is never any ice in any other category, then the solution will be identical to 1CAT. In the second, all newly-formed ice gets nearly evenly distributed amongst all categories resulting in virtually identical sets of properties – and thus subsequent growth rates – in each category, therefore the solution would also be very similar to 1CAT (with tiny difference arising due to changes in order-of-operations calculations, etc.). Thus, any multi-category solution in P3 that is different from the 1-category solution should, in principle, be more physically realistic since it the differences result from being affected by multiple (and different) ice modes and modeling their evolution independently.

Although in this study we extol the benefits of multiple ice-phase categories, this should not be interpreted as a proposal to return to traditional pre-defined category-based schemes. In P3, the categories are not in any way predefined; they all are subject to the identical parameterized process rates and can each represent any type of ice-phase or mixed-phase particle depending on the history of conditions at different locations and times. The merging of two P3 ice categories into one is not comparable to, for example, the conversion from snow to graupel in a traditional scheme. Despite the use of fixed parameters as a proxy for similarity, *merging is not conversion* since it is done between categories that are deemed to be similar, rather than being done to produce a hydrometeor type that is different, as in traditional schemes. A suboptimal P3 configuration, with a poorly chosen similarity criterion, is bound to be less harmful (i.e. result in less sensitivity) than traditional conversion processes based on arbitrary and unconstrained thresholds as was shown, for example, in Morrison & Milbrandt (2011) where there was a large sensitivity of supercell simulations to whether the traditional BMS favored graupel or hail.

Perhaps somewhat ironically, in addition to illustrating the benefits of multi-category P3 for the simulation of hail, the results presented in section 4.2 also strongly support the conclusions originally made in Morrison & Milbrandt (2015) and Morrison et al. (2015) regarding the versatility of using a single free ice-phase category in a BMS to represent a wide range of hydrometeor types and a majority of the important microphysical processes. This is evident from the results since, except for hail in the convective core and near the surface, the overall ice properties in the 1-category simulations (Fig. 7) are similar to those in the multi-category runs (Figs. 12,15).

6 Conclusions

This study examined the impacts of predicting liquid fraction and multiple free ice-phase categories in the P3 microphysics scheme in the context of cloud-resolving, quasi-idealized hailstorm simulations. An important effect of predicting the liquid fraction is to improve the parameterization of melting of ice, in which a portion of the melted mass is temporarily retained in the mixed-phase particles and then gradually shed, depending on the degree of riming. This increases the rate at which ice mass is transferred to rain for heavily-rimed ice for this set of processes and ultimately reduces the amount of hail reaching the surface. In contrast, the impacts of adding ice-phase categories tends to increase the amount of hail reaching the surface, and also the hail sizes. This is due to reduced property dilution, which allows ice to be represented in at least one category as large hail which can reside in the hail growth zone for longer times and thus grow even larger. With multiple categories the dilution of properties is reduced; multiple modes can coexist without loss to either of their sets of properties (with the exception of changes due to category interactions via aggregation) and each population of ice can continue to evolve accordingly. Hailstorm cases from two very different pre-storm environments were used which strengthens the generality of the conclusions regarding the systematic impacts.

Since its inception, the P3 scheme has advanced in terms of its capacity to simulate hail. This includes the implementation of triple-moment ice which controls excessive size sorting, the predicted liquid faction which improves the representation of wet growth, melting, and shedding, and the use of multiple free ice categories which allows hail to grow to large sizes without dilution from smaller particles. Future improvements pertaining to hail will include optimizing the initiation and merging of ice in the multicategory configuration. We also plan to extend the triple-moment treatment of ice to include the formal treatment of all microphysical processes, thereby improving all process rates that impact the dispersion of the size spectra; this will be reported in an upcoming study. On-going improvements to the representation of primary ice nucleation, secondary ice production, and the representation of aerosols is on-going. We believe that the P3 scheme is nearing the point that it can be used as a tool to conduct detailed process studies on hailstorms.

In addition to using P3 as a research tool, all of the results and conclusions on the impacts on simulating hail in this study are valid for km-scale numerical weather prediction (NWP). While all of the simulations presented were done with a 200-m grid spacing to minimize interpretation challenges associated with unresolved deep convection, all of the simulations discussed were also done with a 1-km horizontal grid spacing km (not shown). Each of the sensitivities exhibited at 200 m were similar at 1 km. This is at the scale of some current real-time experimental NWP systems and is at the scale that operational systems are moving towards, even over large areas such as the CONUS. While the configuration of P3 with triple-moment ice, predicted liquid fraction, and two ice categories requires that 18 hydrometeor tracers must be advected and diffused, which would typically be considered computationally prohibitive for operational NWP, microphysics schemes like P3 which have several variables per category lend themselves very well to advection techniques such as the scaled flux vector transport method (SFVT; Morrison et al., 2016). For this specific configuration of P3, 18 microphysics tracers could be advected for the computational cost of advecting 4 primary tracers (one per hydrometeor category) with the standard advection algorithm, plus a relatively small additional cost to compute the advective tendencies of the 14 secondary tracers. Also, due to its extensive use of pre-computed look-up tables, the P3 code itself is quite fast compared to other BMSs (see Morrison et al., 2015). We close in commenting, therefore, that the predictive detail in the LF-2CAT (or even LF-3CAT) configuration could be easily be affordable for a km-scale operational NWP system, even with current computational constraints, using an efficient advection algorithm such as SFVT or artificial-intelligence based advection.

Acknowledgments

We thank George Bryan (NSF NCAR) for developing and maintaining the CM1 model.

Open Research

The code for the P3 scheme, as well as necessary files to interface the latest version with CM1, is available at https://github.com/P3-microphysics/P3-microphysics. The code for the CM1 model is available at https://github.com/NCAR/CM1. The model soundings and namelist files used to generate the simulations are available upon request.

Appendix A

(see Table A1)

Table A1. List of symbols

Symbol	Description	Units
$B_{i,rim}$	rime ice volume mixing ratio (for a given category)	$m^3 kg^{-1}$
D	equivalent diameter	m
$D_{h,max}$	maximum diagnosed hail diameter	m
D_m	mass-weighted mean ice diameter	m
D_{mm}	mean-mass diameter	m
F_{liq}	liquid fraction (for a given ice category)	--
F_{rim}	rime ice mass fraction (for a given category)	--
$N(D)$	number density function (particle size distribution, PSD)	# $m^{-1} kg^{-1}$
N_0	intercept parameter (of gamma PSD)	$m^{-(1+\mu)} kg^{-1}$
$nCat$	number of ice categories	--
N_i	total ice number concentration (for a given category)	# m^{-3}
$N_{i,tot}$	total ice number mixing ratio (for a given category)	# kg^{-1}
Q_c	mass content/concentration of cloud (droplets)	$kg\ m^{-3}$
Q_i	total ice mass concentration/content (for a given category)	$kg\ m^{-3}$
$Q_{i,liq}$	liquid (on ice) mass mixing ratio (for a given category)	$kg\ kg^{-1}$
$Q_{i,rim}$	rime mass mixing ratio	$kg\ kg^{-1}$
$Q_{i,tot}$	total ice mass mixing ratio (for a given category)	$kg\ kg^{-1}$
Q_r	mass content/concentration of rain	$kg\ m^{-3}$
V_m	mass-weighted fall speed for ice	$m\ s^{-1}$
w_{max}	peak updraft speed	$m\ s^{-1}$
Z_{DR}	differential reflectivity (from dual-polarization radar)	dB
Z_e	equivalent reflectivity (from model)	dBZ
$Z_{e,c}$	equivalent reflectivity, column-maximum	dBZ
Z_H	horizontal reflectivity (from radar)	dBZ
$Z_{i,tot}$	reflectivity factor (6^{th} moment) mixing ratio (for a given category)	$m^6 kg^{-1}$
ρ_a	air density	$kg\ m^{-3}$
ρ_i	bulk ice density	$kg\ m^{-3}$
λ	slope parameter (of gamma PSD)	m^{-1}
μ	shape parameter (of gamma PSD)	--

References

Balsara, D. S., & Shu, C. W. (2000). Monotonicity preserving weighted essentially non-oscillatory schemes with increasingly high order of accuracy. *Journal of Computational Physics*, *160*(2), 405-452. https://doi.org/10.1006/jcph.2000.6443

Bryan, G. H., & Fritsch, J. M. (2002). A benchmark simulation for moist nonhydrostatic numerical models. *Monthly Weather Review*, *130*(12), 2917-2928. https://doi.org/10.1175/1520-0493(2002)130<2917:ABSFMN>2.0.CO;2

Chen, J. P., & Tsai, T. C. (2016). Triple-moment modal parameterization for the adaptive growth habit of pristine ice crystals. *Journal of the Atmospheric Sciences*, *73*(5), 2105-2122. https://doi.org/10.1175/JAS-D-15-0220.1

Cholette, M., Morrison, H., Milbrandt, J. A., & Thériault, J. M. (2019). Parameterization of the bulk liquid fraction on mixed-phase particles in the predicted particle properties (P3) scheme: Description and idealized simulations. *Journal of the Atmospheric Sciences*, *76*(2), 561-582. https://doi.org/10.1175/JAS-D-18-0278.1

Cholette, M., Milbrandt, J. A., Morrison, H., Paquin-Ricard, D., & Jacques, D. (2023). Combining Triple-Moment Ice With Prognostic Liquid Fraction in the P3 Microphysics Scheme: Impacts on a Simulated Squall Line. *Journal of Advances in Modeling Earth Systems*, *15*(4), e2022MS003328. https://doi.org/10.1029/2022MS00332

Cholette, M., Milbrandt, J. A., Morrison, H., Kirk, S., & Lalonde, L.É. (2024). Secondary Ice Production Improves Simulations of Freezing Rain. *Geophysical Research Letters*, *in press*.

Dawson, D. T., Mansell, E. R., Jung, Y., Wicker, L. J., Kumjian, M. R., & Xue, M. (2014). Low-level Z DR signatures in supercell forward flanks: The role of size sorting and melting of hail. *Journal of the Atmospheric Sciences*, *71*(1), 276-299. https://doi.org/10.1175/JAS-D-13-0118.1

Deardorff, J. W. (1980). Stratocumulus-capped mixed layers derived from a three-dimensional model. *Boundary-layer meteorology*, *18*, 495-527. https://doi.org/10.1007/BF00119502

Ferrier, B. S. (1994). A double-moment multiple-phase four-class bulk ice scheme. Part I: Description. *Journal of Atmospheric Sciences*, *51*(2), 249-280. https://doi.org/10.1175/1520-0469(1994)051<0249:ADMMPF>2.0.CO;2

Hashino, T., & Tripoli, G. J. (2007). The Spectral Ice Habit Prediction System (SHIPS). Part I: Model description and simulation of the vapor deposition process. *Journal of the Atmospheric Sciences*, *64*(7), 2210-2237. https://doi.org/10.1175/JAS3963.1

Jensen, A. A., Harrington, J. Y., Morrison, H., & Milbrandt, J. A. (2017). Predicting ice shape evolution in a bulk microphysics model. *Journal of the Atmospheric Sciences*, *74*(6), 2081-2104. https://doi.org/10.1175/JAS-D-16-0350.1

Jensen, A. A., Thompson, G., Ikeda, K., & Tessendorf, S. A. (2023). Improving the representation of hail in the Thompson microphysics scheme. *Monthly Weather Review*, *151*(9), 2307-2332. https://doi.org/10.1175/MWR-D-21-0319.1

Johnson, M., Jung, Y., Milbrandt, J. A., Morrison, H., & Xue, M. (2019). Effects of the representation of rimed ice in bulk microphysics schemes on polarimetric signatures. *Monthly Weather Review*, *147*(10), 3785-3810. https://doi.org/10.1175/MWR-D-18-0398.1

Jouan, C., Milbrandt, J. A., Vaillancourt, P. A., Chosson, F., & Morrison, H. (2020). Adaptation of the Predicted Particles Properties (P3) microphysics scheme for large-scale numerical weather prediction. *Weather and Forecasting*, *35*(6), 2541-2565. https://doi.org/10.1175/WAF-D-20-0111.1

Kumjian, M. R., Ryzhkov, A. V., Melnikov, V. M., & Schuur, T. J. (2010). Rapid-scan super-resolution observations of a cyclic supercell with a dual-polarization WSR-88D. *Monthly Weather Review*, *138*(10), 3762-3786. https://doi.org/10.1175/2010MWR3322.1

Lin, Y. L., Farley, R. D., & Orville, H. D. (1983). Bulk parameterization of the snow field in a cloud model. *Journal of Applied Meteorology and Climatology*, *22*(6), 1065-1092. https://doi.org/10.1175/1520-0450(1983)022<1065:BPOTSF>2.0.CO;2

Loftus, A. M., Cotton, W. R., & Carrió, G. G. (2014). A triple-moment hail bulk microphysics scheme. Part I: Description and initial evaluation. *Atmospheric Research*, *149*, 35-57. https://doi.org/10.1016/j.atmosres.2014.05.013

Mansell, E. R., Ziegler, C. L., & Bruning, E. C. (2010). Simulated electrification of a small thunderstorm with two-moment bulk microphysics. *Journal of the Atmospheric Sciences*, *67*(1), 171-194. https://doi.org/10.1175/2009JAS2965.1

Meyers, M. P., Walko, R. L., Harrington, J. Y., & Cotton, W. R. (1997). New RAMS cloud microphysics parameterization. Part II: The two-moment scheme. *Atmospheric Research*, *45*(1), 3-39. https://doi.org/10.1016/S0169-8095(97)00018-5

Milbrandt, J. A., & Yau, M. K. (2005a). A multimoment bulk microphysics parameterization. Part I: Analysis of the role of the spectral shape parameter. *Journal of the Atmospheric Sciences*, *62*(9), 3051-3064. https://doi.org/10.1175/JAS3534.1

Milbrandt, J. A., & Yau, M. K. (2005b). A multimoment bulk microphysics parameterization. Part II: A proposed three-moment closure and scheme description. *Journal of the Atmospheric Sciences*, *62*(9), 3065-3081. https://doi.org/10.1175/JAS3535.1

Milbrandt, J. A., & Morrison, H. (2013). Prediction of graupel density in a bulk microphysics scheme. *Journal of the Atmospheric Sciences*, *70*(2), 410-429. https://doi.org/10.1175/JAS-D-12-0204.1

Milbrandt, J. A., Bélair, S., Faucher, M., Vallée, M., Carrera, M. L., & Glazer, A. (2016). The pan-Canadian high resolution (2.5 km) deterministic prediction system. *Weather and Forecasting*, *31*(6), 1791-1816. https://doi.org/10.1175/WAF-D-16-0035.1

Milbrandt, J. A., & Morrison, H. (2016). Parameterization of cloud microphysics based on the prediction of bulk ice particle properties. Part III: Introduction of multiple free categories. *Journal of the Atmospheric Sciences*, *73*(3), 975-995. https://doi.org/10.1175/JAS-D-15-0204.1

Milbrandt, J. A., Leroyer, S., Paquin-Ricard, D., Faucher, M., Zhang, S., & Jouan, C. (2018). *High resolution deterministic prediction system HRDPS. Update from version 4.4.0 to version 5.0.0* (p. 57). Technical Note, Canadian Meteorological Centre.

Milbrandt, J. A., Morrison, H., Dawson II, D. T., & Paukert, M. (2021). A triple-moment representation of ice in the Predicted Particle Properties (P3) microphysics scheme. *Journal of the Atmospheric Sciences*, *78*(2), 439-458. https://doi.org/10.1175/JAS-D-20-0084.1

Morrison, H. C. J. A., Curry, J. A., & Khvorostyanov, V. I. (2005). A new double-moment microphysics parameterization for application in cloud and climate models. Part I: Description. *Journal of the Atmospheric Sciences*, *62*(6), 1665-1677. https://doi.org/10.1175/JAS3446.1

Morrison, H., Thompson, G., & Tatarskii, V. (2009). Impact of cloud microphysics on the development of trailing stratiform precipitation in a simulated squall line: Comparison of one- and two-moment schemes. *Monthly Weather Review*, *137*(3), 991-1007. https://doi.org/10.1175/2008MWR2556.1

Morrison, H., & Milbrandt, J. (2011). Comparison of two-moment bulk microphysics schemes in idealized supercell thunderstorm simulations. *Monthly Weather Review*, *139*(4), 1103-1130. https://doi.org/10.1175/2010MWR3433.1

Morrison, H., & Milbrandt, J. A. (2015). Parameterization of cloud microphysics based on the prediction of bulk ice particle properties. Part I: Scheme description and idealized tests. *Journal of the Atmospheric Sciences*, *72*(1), 287-311. https://doi.org/10.1175/JAS-D-14-0065.1

Morrison, H., Milbrandt, J. A., Bryan, G. H., Ikeda, K., Tessendorf, S. A., & Thompson, G. (2015). Parameterization of cloud microphysics based on the prediction of bulk ice particle properties. Part II: Case study comparisons with observations and other schemes. *Journal of the Atmospheric Sciences*, *72*(1), 312-339. https://doi.org/10.1175/JAS-D-14-0066.1

Morrison, H., Jensen, A. A., Harrington, J. Y., & Milbrandt, J. A. (2016). Advection of coupled hydrometeor quantities in bulk cloud microphysics schemes. *Monthly Weather Review*, *144*(8), 2809-2829. https://doi.org/10.1175/MWR-D-15-0368.1

Morrison, H., van Lier-Walqui, M., Fridlind, A. M., Grabowski, W. W., Harrington, J. Y., Hoose, C., ... & Xue, L. (2020). Confronting the challenge of modeling cloud and precipitation microphysics. *Journal of Advances in Modeling Earth Systems*, *12*(8), e2019MS001689. https://doi.org/10.1029/2019MS00168

Murakami, M. (1990). Numerical modeling of dynamical and microphysical evolution of an isolated convective cloud The 19 July 1981 CCOPE cloud. *Journal of the Meteorological Society of Japan. Ser. II*, *68*(2), 107-128. https://doi.org/10.2151/jmsj1965.68.2_107

Naylor, J., & Gilmore, M. S. (2012). Convective initiation in an idealized cloud model using an updraft nudging technique. *Monthly Weather Review*, *140*(11), 3699-3705. https://doi.org/10.1175/MWR-D-12-00163.1

Park, S. Y., Lim, K. S. S., Kim, K., Lee, G., & Milbrandt, J. A. (2024). Introduction of Prognostic Graupel Density in Weather Research and Forecasting (WRF) Double-Moment 6-Class (WDM6) Microphysics and Evaluation of the Modified Scheme During the ICE-POP Field Campaign. *Geoscientific Model Development Discussions*, *2024*, 1-29. https://doi.org/10.5194/gmd-2023-241

Paukert, M., Fan, J., Rasch, P. J., Morrison, H., Milbrandt, J. A., Shpund, J., & Khain, A. (2019). Three-moment representation of rain in a bulk microphysics model. *Journal of Advances in Modeling Earth Systems*, *11*(1), 257-277. https://doi.org/10.1029/2018MS001512

Qu, Z., Korolev, A., Milbrandt, J. A., Heckman, I., Huang, Y., McFarquhar, G. M., Morrison, H., Wolde, M. & Nguyen, C. (2022). The impacts of secondary ice production on microphysics and dynamics in tropical convection. *Atmospheric Chemistry and Physics*, *22*(18), 12287-12310. https://doi.org/10.5194/acp-22-12287-2022

Reisner, J., Rasmussen, R. M., & Bruintjes, R. T. (1998). Explicit forecasting of supercooled liquid water in winter storms using the MM5 mesoscale model. *Quarterly Journal of the Royal Meteorological Society*, *124*(548), 1071-1107. https://doi.org/10.1002/qj.49712454804

Rutledge, S. A., & Hobbs, P. (1983). The mesoscale and microscale structure and organization of clouds and precipitation in midlatitude cyclones. VIII: A model for the “seeder-feeder” process in warm-frontal rainbands. *Journal of the Atmospheric Sciences*, *40*(5), 1185-1206. https://doi.org/10.1175/1520-0469(1983)040<1185:TMAMSA>2.0.CO;2

Seifert, A., & Beheng, K. D. (2006). A two-moment cloud microphysics parameterization for mixed-phase clouds. Part 1: Model description. *Meteorology and Atmospheric Physics*, *92*(1), 45-66. https://doi.org/10.1007/s00703-005-0112-4

Skamarock, W. C., Klemp, J. B., Dudhia, J., Gill, D. O., Barker, D. M., Duda, M. G., ... & Powers, J. G. (2008). A description of the advanced research WRF version 3. *NCAR technical note*, *475*, 113.

Thompson, G., & Eidhammer, T. (2014). A study of aerosol impacts on clouds and precipitation development in a large winter cyclone. *Journal of the Atmospheric Sciences*, *71*(10), 3636-3658. https://doi.org/10.1175/JAS-D-13-0305.1

Tsai, T. C., & Chen, J. P. (2020). Multimoment ice bulk microphysics scheme with consideration for particle shape and apparent density. Part I: Methodology and idealized simulation. *Journal of the Atmospheric Sciences*, *77*(5), 1821-1850. https://doi.org/10.1175/JAS-D-19-0125.1

Wang, J., Fan, J., Feng, Z., Zhang, K., Roesler, E., Hillman, B., ... & Xie, S. (2021). Impact of a new cloud microphysics parameterization on the simulations of mesoscale convective systems in E3SM. *Journal of Advances in Modeling Earth Systems*, *13*(11), e2021MS002628. https://doi.org/10.1029/2021MS002628

Xue, L., Fan, J., Lebo, Z. J., Wu, W., Morrison, H., Grabowski, W. W., ... & Rasmussen, R. M. (2017). Idealized simulations of a squall line from the MC3E field campaign applying three bin microphysics schemes: Dynamic and thermodynamic structure. *Monthly Weather Review*, *145*(12), 4789-4812. https://doi.org/10.1175/MWR-D-16-0385.1

Yang, J., & Yau, M. K. (2008). A new triple-moment blowing snow model. *Boundary-layer meteorology*, *126*, 137-155. https://doi.org/10.1007/s10546-007-9215-4

Young, K. C., 1993: *Microphysical Processes in Clouds*, Oxford University Press, Inc. 427 pp.

Ziegler, C. L. (1985). Retrieval of thermal and microphysical variables in observed convective storms. Part 1: Model development and preliminary testing. *Journal of the Atmospheric Sciences*, *42*(14), 1487-1509. https://doi.org/10.1175/1520-0469(1985)042<1487:ROTAMV>2.0.CO;2